

1 **Part 2. Elemental composition, iron mineralogy and**  
2 **solubility of anthropogenic and natural mineral dust**  
3 **aerosols in Namibia: a case study analysis from the**  
4 **AEROCLO-sA campaign**

5  
6 Paola Formenti<sup>1\*</sup>, Chiara Giorio<sup>2,3</sup>, Karine Desboeufs<sup>1</sup>, Alexander Zherebker<sup>2</sup>, Marco Gaetani<sup>4</sup>,  
7 Clarissa Baldo<sup>5</sup>, Gautier Landrot<sup>6</sup>, Simona Montebello<sup>2,7</sup>, Servanne Chevallier<sup>1</sup>, Sylvain  
8 Triquet<sup>1</sup>, Guillaume Siour<sup>5</sup>, Claudia Di Biagio<sup>1</sup>, Francesco Battaglia<sup>1</sup>, Jean-François Doussin<sup>5</sup>,  
9 Anais Feron<sup>1,§</sup>, Andreas Namwoonde<sup>8</sup>, and Stuart Piketh<sup>9</sup>

10  
11 <sup>1</sup> Université Paris Cité and Univ. Paris Est Creteil, CNRS, LISA, F-75013 Paris, France

12 <sup>2</sup> Yusuf Hamied Department of Chemistry, University of Cambridge, Lensfield Road,  
13 Cambridge, CB2 1EW, United Kingdom

14 <sup>3</sup> Dipartimento di Scienze Chimiche, Università degli Studi di Padova, 35131 Padova, Italy

15 <sup>4</sup> Classe di Scienze Tecnologie e Società, Scuola Universitaria Superiore IUSS, 27100, Pavia,  
16 Italia

17 <sup>5</sup> Univ Paris Est Creteil and Université Paris Cité, CNRS, LISA, F-94010 Créteil, France

18 <sup>6</sup> Synchrotron SOLEIL, L'Orme des Merisiers, Saint-Aubin, France

19 <sup>7</sup> Department of Engineering 'Enzo Ferrari', University of Modena and Reggio Emilia, 41125  
20 Modena, Italy

21 <sup>8</sup> Sam Nujoma Marine and Coastal Resources Research Centre, University of Namibia,  
22 Henties Bay, Namibia

23 <sup>9</sup> NorthWest University, Potchefstroom, South Africa

24 <sup>§</sup> now at INRAE

25  
26  
27 \*Correspondence to: [paola.formenti@lisa.ipsl.fr](mailto:paola.formenti@lisa.ipsl.fr)

28  
29 **Abstract**

30 This paper presents the results of three weeks of aerosol sampling at the Henties Bay coastal  
31 site in Namibia during the Aerosols, Radiation and Clouds in southern Africa (AEROCLO-sA)  
32 field campaign in August-September 2017. The campaign coincided with a transition period  
33 between two synoptic regimes and corresponded to a significant change in the aerosol  
34 composition measured at the site and in particular of that of mineral dust. During August, the  
35 dust was natural windblown from the southerly gravel plains with a composition consistent with  
36 that previously observed in Namibia. In September, the dust was fugitive from anthropogenic  
37 mining and possibly minor contribution of smelting emissions in northern Namibia or as far as  
38 the Copper Belt in Zambia, one of the regional hotspot of pollution.

39 Chemical analysis of filter samples highlights the difference in elemental composition, in  
40 particular heavy metals, such as As, Cu, Cd, Pb, and Zn, but also silicon, in the anthropogenic  
41 dust. The metal solubility of the natural dust was higher, including that of iron (up to 5%  
42 compared to less than 1% for anthropogenic dust). Anthropogenic dust ~~In addition~~was  
43 associated with slight ~~to the~~ higher content of iron oxides and ~~the a~~ larger proportion of coarse  
44 particlessize of particles in the anthropogenic dust. Additionally, we ~~we~~ found that the iron  
45 solubility, and, more in general, the metals' solubility, correlated to the high concentrations of  
46 fluoride ion which are attributed to marine emissions from the Namibian shelf. These results  
47 highlight in a renewed manner the importance of ocean-atmosphere exchanges affecting both  
48 the atmospheric composition and the marine biogeochemistry in the Benguela region.

## 49 **1 Introduction**

50 Mineral dust is an abundant component of the global atmosphere (Kok et al., 2023). Dust  
51 particles in the atmosphere are released by the natural wind erosion of natural arid and semi-  
52 arid areas of the globe. However, between 20 and 30% of the global dust emissions are is also  
53 contributed by anthropogenic activities such as labouring of bare soils for agriculture, pasture  
54 or construction, but also fugitive dust from mining and road traffic activities (Knippertz and  
55 Stuut, 2014; Chen et al., 2023). Mineral dust is a strong regulator of the Earth's climate and  
56 environment (Kok et al., 2023). In the atmosphere, it contributes to both the direct and indirect  
57 radiative effects on climate by scattering and absorbing solar and terrestrial radiation and  
58 forming cloud droplets in the liquid and ice phases (Kok et al., 2023). It also affects the  
59 atmospheric composition and oxidative capacity by acting as a source or a reactive sink of  
60 species from the gas phase (Usher et al., 2003). It also acts as an irritating agent for the upper  
61 respiratory system and a vector of bacteria and infections (Adebiyi et al., 2023). By deposition,  
62 mineral dust can provide nutrients and pollutants to the sea water, changing the ocean's  
63 primary production (Knippertz and Stuut, 2014).

64 These considerations apply to the west coast of southern Africa, and Namibia in particular, a  
65 hyper-arid climate where many dust sources co-exist (Vickery et al., 2013). Natural mineral  
66 dust is emitted from coastal riverine sources, salty pans such as the Etosha and large gravel  
67 plains ubiquitous around the country (Vickery et al., 2013; Dansie et al., 2017; Von Holdt et al.,  
68 2018; Klopper et al., 2020; Shikwambana and Kganyago, 2022; Desboeufs et al., 2024). These  
69 sources are active throughout the year as emissions occur under various wind regimes (Von  
70 Holdt et al., 2018). Natural mineral dust from Namibia is transported within the shallow  
71 boundary layer but being able to reach as far as Eastern Antarctica through long-range  
72 transport (Gili et al., 2022). Previous research in Namibia has shown that natural mineral dust  
73 from the coastal riverbeds and the gravel plains might contribute to oceanic productivity,  
74 particularly along the coast (Dansie et al., 2022). This research also pointed to iron as a highly

75 soluble element in both the soil and windblown aerosol fraction and the control for the impact  
76 of dust on oceanic productivity (Dansie et al., 2017a; 2017b; 2018; Desboeufs et al., 2024).

77 Furthermore, coastal pollution is an emerging issue of the present-day world (Strain et al.,  
78 2022). Increased human activities and coastal developments are quickly affecting the air  
79 quality but also the aquatic environment and biodiversity (Micella et al., 2024). Indeed, and  
80 despite its low population, Namibia also has intense and emerging economic activities such as  
81 mining (various heavy elements, including uranium; Mileusnić et al., 2014; Sracek, 2015;  
82 Liebenberg-Enslin et al., 2020) and marine traffic transporting merchandise along the coast of  
83 Africa and towards South America (Tournadre, 2014; Klopper et al., 2020). These activities  
84 release fugitive dust from the mine locations as well as from the numerous road constructions  
85 from and to the major national harbour, Walvis Bay (<https://mwt.gov.na/projects>; last accessed  
86 26/11/2024). In Namibia, the accumulation of heavy metals in the shore and coastal waters  
87 due to coastal mining (Onjefu et al., 2020) has been previously documented (Sylvanus et al.,  
88 2016; Omoregie et al., 2019; Nekhoroshkov et al., 2021). Furthermore, in the austral  
89 wintertime, Namibia is affected by anti-cyclonic circulation, resulting in the transport of light-  
90 absorbing particles, likely from forest fires and mining areas such as the Zambian Copper Belt  
91 (Formenti et al., 2018; Aurélien et al., 2022; Martinez-Alonso et al., 2023; Křibek et al., 2023).  
92 The composition of these emissions is little characterised to date while having the potential for  
93 alter the oceanic productivity and microbial biogeochemistry (Adriano, 2001; Jordi et al., 2012;  
94 Mahowald et al., 2018; Yang et al. 2019).

95 In this paper, we present a case study analysis of the differences and similarities of the  
96 composition of natural and anthropogenic mineral dust sampled during the ground-based field  
97 campaign of the Aerosols, Radiation and Clouds in southern Africa (AEROCLO-sA) project  
98 (Formenti et al., 2019). The campaign was conducted in August-September 2017 in Henties  
99 Bay (22°6'S, 14°30'E; 20 m above mean sea level) along the Namibian coast.

100 Based on analysis of the chemical composition and meteorological fields, we demonstrate the  
101 origin of the anthropogenic dust and contrast its elemental composition, iron mineralogy and  
102 solubility, and the type of organic matter with respect to that of natural dust measured at the  
103 beginning of the campaign. Our analysis focusses on the iron mineralogy and solubility but  
104 includes, for the first time the evaluation of the solubility of heavy metals transported with these  
105 emissions.

## 106 **2 Experimental**

107 The AEROCLO-sA field campaign took place from 21 August to 13 September 2017 at the  
108 Sam Nujoma Marine and Coastal Resources Research Centre (SANUMARC) of the University  
109 of Namibia at Henties Bay (Formenti et al., 2019). This sampling site, operated on the long-

110 term as described by Formenti et al. (2018) and Klopper et al. (2020), was augmented with the  
111 PortabIE Gas and Aerosol Sampling UnitS (PEGASUS; <https://pegasus.aeris-data.fr/>; last  
112 accessed 24/01/2025) mobile facility for the time of the campaign.

113 The PEGASUS facility consists of two marine containers (20-feet long) customized and  
114 equipped for atmospheric research (Formenti et al., 2019). Air sampling is performed with two  
115 high-volume aerosol inlets delivering approximately 450 L min<sup>-1</sup> each. At wind speeds between  
116 5 to 10 m s<sup>-1</sup>, typical for coastal Namibia (see Figure S1), sampling is almost isokinetic for  
117 particles up to 40 µm in aerodynamic diameter (Rajot et al., 2008), which hereafter we named  
118 total suspended particulate (TSP). The total sampled flow rate is distributed to online analysers  
119 and to multiple- and single-stack sample collection units for off-line analysis of the bulk and  
120 size-resolved chemical and mineralogical composition, soluble fraction and mixing state. The  
121 details of the online instrumentation relevant to this publication are listed in Table S1 in the  
122 supplementary material.

## 123 **2.1 Sample collection**

124 During the campaign, aerosol samples were collected both during day (approximately 07:00-  
125 17:00 UTC) and night time (approximately 17:30-06:30 UTC). The sampling duration was  
126 marginally adapted in real-time to the nature and the aerosol load of air masses using the  
127 readings of the local wind speed and direction and of the aerosol mass concentration, also  
128 measured online.

129 Four custom-made filter holders were used in parallel for collecting aerosols in the TSP  
130 fraction. These were loaded with (i) one Teflon filter (Zefluor®, 2-µm pore size diameter, 47-  
131 mm filter diameter); (ii) two polycarbonate membranes (Nuclepore®, 0.4-µm pore size  
132 diameter, 37-mm and 47-mm filter diameter, respectively), and (iii) a quartz filter (Pall,  
133 2500QAT-UP Tissuquartz, 47-mm filter diameter). The average sampling flow rate varied  
134 between 20 and 30 L min<sup>-1</sup>.

135 Two samples of the composition of particles smaller than 1 µm in diameter (hereafter named  
136 PM<sub>1</sub> size fraction) were collected in parallel using two 4-stage Dekati® PM<sub>10</sub> Impactors, both  
137 operated at 10 L min<sup>-1</sup>. For these two samplers we used 25-mm polycarbonate membranes on  
138 three impactor stages (> 10 µm, 10-2.5 µm and 2.5-1 µm) while the final filter stage, where the  
139 PM<sub>1</sub> fraction is collected, was a polycarbonate membrane (Nuclepore®, 0.4-µm pore size, 47-  
140 mm filter diameter) and a quartz filter (Pall, 2500QAT-UP Tissuquartz, 47-mm filter diameter),  
141 respectively.

142 Before the campaign, Teflon and quartz membranes were cleaned for sampling organic  
143 aerosols. Teflon membranes were rinsed with dichloromethane and baked at 100°C for 10  
144 minutes. Quartz membranes were baked at 550°C for 12 hours. Both were conditioned in pre-

145 baked aluminium foils. The polycarbonate membranes were used for measuring the inorganic  
146 and water-soluble fraction composition. The 37-mm and 25-mm membranes were used as  
147 purchased, while the 47-mm ones were acid-washed according to the protocol described in  
148 Desboeufs et al. (2024). All material was sealed and opened only before collection.  
149 Immediately after exposure, all samples were sealed and stored at -18°C in the deep-freezer  
150 available in the PEGASUS facility, from which they were transported back to the laboratory.

151 TSP filter samples were collected between 21 August and 12 September 2017, while PM<sub>1</sub>  
152 samples were collected from 26 August 2017 onwards. In total, 36 TSP and 31 PM<sub>1</sub> samples  
153 were collected per filter type during the field campaign (including blanks).

## 154 2.2 Sample analysis

### 155 2.2.1 Elements and water-soluble ions

156 The analysis of the elemental and water-soluble ion concentrations was performed at LISA  
157 according to the protocols previously detailed in Klopper et al. (2020) and Desboeufs et al.  
158 (2024). The elemental concentrations of 24 elements (Na, Mg, Al, Si, P, S, Cl, K, Ca, Ti, V, Cr,  
159 Mn, Fe, Co, Ni, Cu, Zn, As, Sr, Pb, Nd, Cd, Ba) were measured by wavelength-dispersive X-  
160 ray fluorescence (WD-XRF) using a PW-2404 spectrometer (Panalytical, Almelo,  
161 Netherlands). The instrument was calibrated with mono- and bi-elemental certified elemental  
162 standards (Micromatter Inc., Surrey, Canada). The concentrations of light-weight elements (Na  
163 to Ca) in the TSP fraction were corrected for X-ray self-attenuation as described in Formenti  
164 et al. (2010), assuming a mean diameter of 4.5 µm to represent the average coarse particle  
165 size. Elements heavier than Ca, as well as concentrations measured in the PM<sub>1</sub> fraction, were  
166 not corrected. The measured atmospheric concentrations are expressed in ng m<sup>-3</sup>, and the  
167 relative analytical uncertainty was evaluated as 10 % ([see Klopper et al. \(2020\) for the full](#)  
168 [description](#)).

169 The analysis of the water-soluble fraction was performed by extracting the filters with 20 mL of  
170 ultrapure water (MilliQ® 18.2 MΩ.cm) for 30 minutes. The solution was divided into two sub-  
171 samples filtered to 0.2 µm of porosity (Nuclepore). One half was analyzed by ion  
172 chromatography (IC) using a Metrohm IC 850 device equipped with a column MetrosepA supp  
173 7 (250/4.0 mm) for anions and with a Metrosep C4 (250/4.0 mm) for cations. The IC analysis  
174 provided the concentrations of the following water-soluble ions: F<sup>-</sup>, formate, acetate, MSA<sup>-</sup>  
175 (methanesulphonic acid), Cl<sup>-</sup>, NO<sub>3</sub><sup>-</sup>, SO<sub>4</sub><sup>2-</sup>, oxalate, Na<sup>+</sup>, NH<sub>4</sub><sup>+</sup>, K<sup>+</sup>, Ca<sup>2+</sup> and Mg<sup>2+</sup>. A calibration  
176 with certified standard multi-ions solutions of concentrations ranging from 5 to 5000 ppb was  
177 performed and, the uncertainty of the analysis was estimated to be 5% ([Klopper et al., 2020](#)).

178 The second half of the solution was acidified to 1% with ultrapure nitric acid (HNO<sub>3</sub>) and  
179 analysed by a combination of inductively coupled plasma-atomic emission spectroscopy (ICP

180 AES) using Spectro ARCOS Ametek® ICP-AES and by high-resolution inductively coupled  
181 plasma-mass spectrometry (HR-ICP-MS) using a Neptune Plus™ instrument by Thermo  
182 Scientific™ as described in Desboeufs et al. (2024). The calibration curve was performed using  
183 standard multi-element solutions ranging from 1 to 1000 ppt. The elemental fractional solubility  
184 (FS) for element is calculated as the ratio between the dissolved and the total concentration.

185 Organic carbon (OC) and elemental carbon (EC) were measured using a thermo-optical  
186 carbon analyser (Sunset Laboratory Inc.) on a 1.5 cm<sup>2</sup> filter following the EUSSAR-II protocol  
187 (Cavalli et al., 2010). The Sunset analyzer was calibrated using a sucrose solution (purity >  
188 99.5 %) in the concentration range between 0.42 µg cm<sup>-2</sup> and 40 µg cm<sup>-2</sup>. The limit of  
189 quantification for total carbon and organic carbon is henceforth estimated to be equal to 0.42  
190 µg cm<sup>-2</sup>. An instrumental blank and a control point with a sucrose solution at 10 µg cm<sup>-2</sup> were  
191 done at the beginning of each day of analysis. OC and EC concentrations are automatically  
192 calculated with the software OCBC835 (Sunset Laboratory). The optical split point was  
193 manually verified to ensure their assignment.

194 All the concentration values presented in this paper were corrected for the average  
195 concentration measured for their corresponding analytical blanks, which was almost equal to  
196 the limit of detection.

### 197 **2.2.2 Iron mineralogy**

198 The quantification of iron oxides and the partitioning of iron species in the II- and III-oxidation  
199 state was performed by X-Ray Absorption (XAS) analysis at the Fe K-edge. Analysis was  
200 performed on the Teflon TSP filters only as the concentrations of the PM<sub>1</sub> filters were not high  
201 enough for this kind of analysis.

202 XAS analysis was conducted at the SAMBA (Spectroscopies Applied to Materials based on  
203 Absorption) line at the SOLEIL synchrotron facility in Saclay, France (Briois et al., 2011)  
204 according to the protocols and procedures previously presented in Formenti et al. (2014) and  
205 Caponi et al. (2017). A Si(220) double-crystal monochromator was used to produce a  
206 monochromatic X-ray beam, which was 4000 x 1000 µm<sup>2</sup> in size at the focal point. The energy  
207 of the X-ray beam was calibrated with an external Fe foil standard before the experiments. The  
208 energy range was scanned from 7050 eV to 7350 eV at a step resolution of 0.2 eV.

209 Aerosol samples were mounted in an external setup. A portion of each aerosol filter sample  
210 was cut and mounted on a carton board holder with 5 available positions and analysed in  
211 fluorescence mode without prior preparation. The number of scans per sample was set  
212 between 50 and 200, depending on the iron concentration, to improve the signal-to-noise ratio.  
213 One scan acquisition lasted approximately 100 seconds for a total of 1.3 hours to 5.5 hours of  
214 measurements for 50 to 200 scans.

215 The spectral analysis was conducted with the FASTOSH software package developed at  
216 SAMBA. As described in Wilke et al. (2001) and O'Day et al. (2004), the oxidation state and  
217 the bonding environment of Fe in dust samples give rise to different features in the XAS  
218 spectra. In the pre-edge region, the shape of the XAS spectra is determined by electronic  
219 transitions to empty bound states, which are strongly influenced by the oxidation state of the  
220 absorbing atom but also by the local geometry around the absorbing atom due to hybridization  
221 effects. Wilke et al. (2001) found that for Fe(II)-bearing minerals, the position of the centroid of  
222 the pre-edge is found at 7112.1 eV, whereas it is at 7113.5 eV for Fe(III)-bearing minerals. The  
223 position of the rising edge, which also depends on the oxidation state, is found at approximately  
224 7120 eV. In the X-ray Absorption Near Edge Structure (XANES) region, extending  
225 approximately 50 eV above the K-edge peak, features are determined by multiple-scattering  
226 resonances of the photo-electron ejected at low kinetic energies.

227 The speciation of Fe was obtained by the least-square fit of the measured XANES spectra  
228 based on the linear combination of mineralogical references. Fits were conducted on the first  
229 derivative of the normalized spectral absorbance in the energy region between 7100 to 7180  
230 eV, corresponding to -30 and +50 eV of the K-edge. Only the fits with a  $\chi^2$  closest to 1 were  
231 retained for further analysis.

232 The reference standards were chosen based on the expected iron mineralogy in the area  
233 (White et al., 2007; Heine and Völkel, 2010; Formenti et al., 2014; Sracek, 2015; Zhang et al.,  
234 2022). Standards for clays (illite and montmorillonite) and iron oxides as goethite, magnetite  
235 and hematite were taken from Formenti et al (2014) and Baldo et al. (2020). The ferrihydrite  
236 standard was derived by the database of the Advanced Light Source, Lawrence Berkeley  
237 National Lab (S. Frakra, pers. comm.). Standards for metal-ligand complexes expected to form  
238 in fog droplets and deliquescent aerosol at high RH (Giorio et al., 2022) is provided in Table  
239 S2 in the supplementary material.

### 240 **2.2.3 Organic analysis**

241 The water-soluble fraction of organic aerosols (WSOC) was extracted, purified using  
242 hydrophobic resin (Bond Elut ppl) and analysed by high-resolution mass spectrometry (HRMS)  
243 namely by hybrid LTQ-Orbitrap equipped with electrospray source (ESI) operated in negative  
244 ion mode. All the samples were directly injected into the ESI source using a syringe pump. In  
245 each case spectra were recorded in triplicates in two mass diapasons to decrease the number  
246 of ions in the detector: 50-500 m/z and 150-700 m/z. Raw spectra were treated following the  
247 laboratory procedure reported in Zhrebker et al. (2024). Files were converted to \*.mzML  
248 format using msconvert with vendor-recommended peak-picking algorithm  
249 (<https://proteowizard.sourceforge.io/>; last accessed 18/12/2024), which was suitable for a

250 series of in-house written Python scripts which included de-noising, calibration, formulae  
251 assignment, and blank subtraction. Only formulae presented in triplicates were retained.  
252 Diapasons were combined with removing lower-intensity duplicates. Formulae assignment  
253 was performed considering only single-charged ions, ignoring anion-radicals with the following  
254 atomic constraints: O/C ratio  $\leq 2$ ,  $0.3 < \text{H/C ratio} < 2.5$ ; element counts [ $1 < C \leq 60$ ,  $2 < H \leq$   
255  $100$ ,  $0 < O \leq 60$ ,  $N \leq 2$ ,  $S \leq 1$ ]. Each formula was attributed to the tentative chemical class  
256 (Table S4) based on the constrained aromaticity index ( $AI_{\text{con}}$ ) calculated according to  
257 Zherebker et al. (2022). In addition, the double bond equivalent (DBE) has been calculated,  
258 which represents the sum of  $sp^2$  and  $sp$  bonds and cycles. Further details of the mass-  
259 spectrometry results are provided in Text S1 in the supplementary material.

## 260 **2.3 Ancillary products**

### 261 **2.3.1 Air mass back trajectories**

262 Three-dimensional air mass back-trajectories ensemble are calculated using the NOAA HYbrid  
263 Single-Particle Lagrangian Integrated Trajectory Model (HYSPLIT; Draxler and Rolph, 2015).  
264 Weather Research Forecasting Model (WRF, version 3.7.1; Skamarock et al., 2008) forced by  
265 Operational Global Analysis data (NCEP: National Centers for Environmental Prediction;  
266 GDAS: Global Data Assimilation System, <https://rda.ucar.edu/datasets/d083002>, last  
267 accessed 10/01/2025) was used to simulated hourly meteorological data at 50km and 9km  
268 horizontal resolution.

### 269 **2.3.2 Atmospheric circulation**

270 The atmospheric circulation and composition at the regional scale from 21 August to 13  
271 September 2017 was further investigated using the Copernicus Atmospheric Monitoring  
272 Service (CAMS) reanalysis (Inness et al., 2019), available every 3 h from 00:00 to 21:00 UTC.  
273 The spatial resolution is approximately 80 km and 60 pressure levels (37 of which are below  
274 20 km and 20 below 5 km). The atmospheric composition is described by analysing the total  
275 aerosol optical depth (AOD) at 550 nm and the mass mixing ratio of dust and sulphate  
276 aerosols. The atmospheric circulation is described by analysing the near-surface (10 m) wind,  
277 to highlight emission processes and local transport, and the geopotential height at 700 hPa, to  
278 highlight the large-scale circulation and long-range transport. Atmospheric composition and  
279 circulation data are averaged at the daily time scale.

### 280 **2.3.3 Positive matrix factorisation analysis**

281 Positive Matrix Factorisation (PMF) (Paatero, 1997; Paatero and Tapper, 1994) was applied  
282 to chemical composition data (OC, EC, inorganic ions and total metals) of TSP and  $PM_{10}$   
283 samples using the software EPA PMF 5.0. Different factor solutions were investigated in the  
284 range of 3 to 8 factors, starting from 10 different seeds. The 4-factor solution and the 3-factor

285 solution were selected for TSP and PM<sub>1</sub>, respectively, based on the inflexion point of Q/Q<sub>exp</sub>  
286 and chemical interpretation of the resulting factor profiles (loadings). The selected solutions  
287 were run again from 100 different seeds, and the solutions with the lowest Q were selected.  
288 Rotational ambiguity was investigated by changing the F<sub>peak</sub> parameter from 0 to ± 0.5 and ±  
289 1. The solutions with F<sub>peak</sub> = 0 were selected, and bootstrap analysis was performed using a  
290 number of bootstraps of 100 and a minimum r-value of 0.6.

## 291 **3 Results**

### 292 **3.1 Air mass origin and local meteorology**

293 Chazette et al. (2019) and Gaetani et al. (2021) showed that mid-tropospheric air masses  
294 during the field campaign were characterized by three distinct periods. A first period (P1; 22–  
295 28 August 2017) when air masses were southerly and characterized by low aerosol content  
296 and large particles. From 23 to 25 August, the circulation in the middle troposphere was  
297 characterized by the reinforcement of the South Atlantic anticyclone, leading to prevailing  
298 south-westerly winds above Namibia (Figure S2). From 26 to 28 August, the transit of a  
299 disturbance in the Southern Ocean was accompanied by the installation of the continental high  
300 and prevailing north-westerly winds above Namibia (Figure S2). A second period (P2; 29  
301 August–1 September 2017) when the circulation was characterized by the weakening of the  
302 South Atlantic anticyclone and the reinforcement of the continental high (Figure S2),  
303 associated with a northerly/easterly flow and transport of recirculation of a higher load of  
304 aerosols associated with biomass burning. The circulation pattern remained the same on the  
305 third period (P3; 3–12 September 2017), but the aerosol content further increased. After the  
306 transit of a cut-off low in the upper troposphere on 2-4 September (Flamant et al., 2022), the  
307 large-scale circulation was dominated by the further reinforcement of the continental high and,  
308 on the 8-9 September, by the installation of a trough over the South Atlantic, leading to  
309 favourable conditions for the recirculation of continental aerosol towards Namibia.

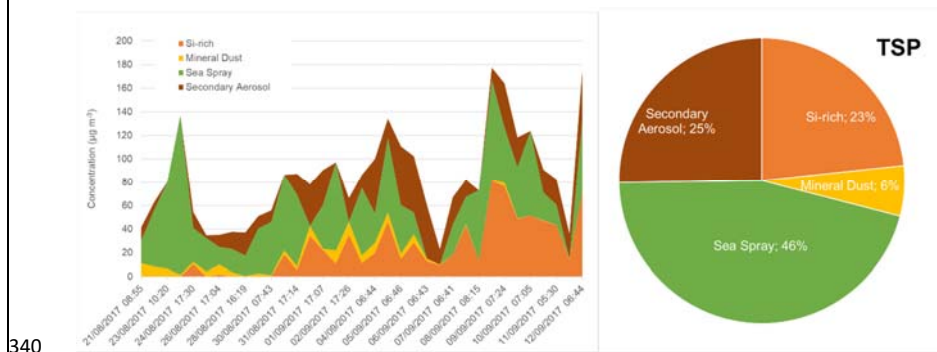
310 The same synoptic circulation was observed at the surface level. Air mass back trajectories  
311 (Figure S3) show that the air flow at the surface level was southerly during P1 and P2 but  
312 shifted to north-easterly (continental) after 2 September (P3), when the frequency of the anti-  
313 cyclonic circulation towards Henties Bay increased. Continental air masses generally took  
314 more than 2 days to reach the site. In the last two days of transport, they moved along the  
315 coast or recirculated around Henties Bay, alternating the S-SW and NW-NNW directions. In a  
316 few cases, and in particular on 11 September, the transport of continental air masses was  
317 more direct and within two days from Henties Bay. The record of local winds measured during  
318 the campaign (Figure S1 in the supplementary material) testifies of the frequent recirculation.  
319 Strong winds (average 5 m s<sup>-1</sup>, and up to 10 m s<sup>-1</sup>) came, alternatively, from the S-SW direction

320 (20-22 August, 29-31 August, 6-9 September, 11 September, grey boxes in Figure S1) and  
321 the NW-NNW direction (23-28 August, 1-5 September, 10 September, 12-13 September).  
322 Occasionally, a gentle land breeze (easterly winds below  $2 \text{ m s}^{-1}$ ) was observed before sunrise  
323 or after sunset. In general terms, as discussed in Giorio et al. (2022), the local meteorological  
324 conditions at Henties Bay during the campaign were characterized by remarkable stability in  
325 terms of temperature (around  $12 \text{ }^{\circ}\text{C}$ ) and humidity (RH  $\sim 95\%$ ), while a persistent stratocumulus  
326 cloud deck kept solar irradiance below  $600 \text{ W m}^{-2}$ .

### 327 3.2 Aerosol composition and origin

328 The summary statistics of the aerosol composition is reported in Table S3 as supplementary  
329 information. The TSP chemical composition was dominated by the sea salt tracers,  $\text{Na}^+$  and  
330  $\text{Cl}^-$  (average  $\pm$  standard deviation concentrations of  $22 \pm 11 \text{ } \mu\text{g m}^{-3}$  and  $39 \pm 21 \text{ } \mu\text{g m}^{-3}$ ,  
331 respectively), as well as  $\text{SO}_4^{2-}$  ( $9.1 \pm 4.3 \text{ } \mu\text{g m}^{-3}$ ),  $\text{Mg}^{2+}$  ( $3.9 \pm 2.0 \text{ } \mu\text{g m}^{-3}$ ),  $\text{K}^+$  ( $1.2 \pm 0.6 \text{ } \mu\text{g m}^{-3}$ )  
332 and  $\text{Ca}^{2+}$  ( $1.7 \pm 0.8 \text{ } \mu\text{g m}^{-3}$ ). In terms of metals and metalloids, Al ( $0.6 \pm 0.4 \text{ } \mu\text{g m}^{-3}$ ), Fe ( $0.6 \pm$   
333  $0.4 \text{ } \mu\text{g m}^{-3}$ ), and Si ( $2.5 \pm 1.3 \text{ } \mu\text{g m}^{-3}$ ) had the highest concentrations. The mean OC and EC  
334 concentrations were  $3.2 \pm 1.5 \text{ } \mu\text{g m}^{-3}$  and  $0.2 \pm 0.2 \text{ } \mu\text{g m}^{-3}$ , respectively. ~~The concentrations of~~  
335 ~~methanesulfonic acid (MSA), tracer of marine biogenic productivity, averaged at  $61 \pm 26 \text{ ng}$~~   
336  ~~$\text{m}^{-3}$ .~~ In the  $\text{PM}_{10}$  fraction, due to the low flow rate used for sampling ( $10 \text{ L min}^{-1}$ ), only the major  
337 elements and ions were detected, in lower c- Concentrations in the  $\text{PM}_{10}$  fraction were generally  
338 lower than in the TSP.

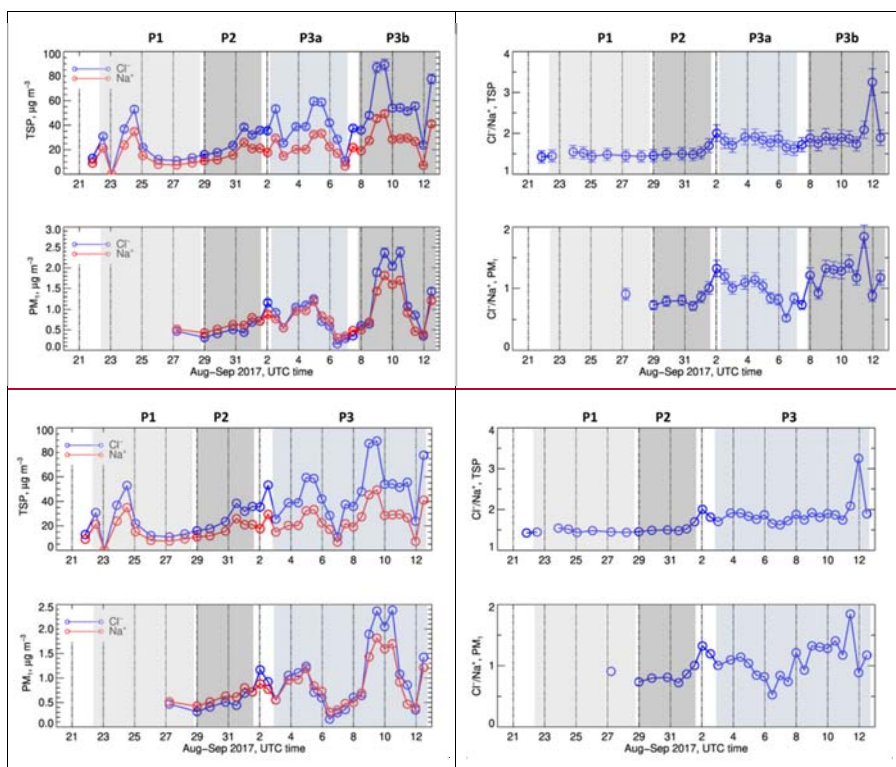
339 These observations are reflected in the results of the PMF analysis shown in Figure 1.





367 **3.2.1 Marine aerosols**

368 Figure 4-2 presents the time series of the elemental concentrations of Na<sup>+</sup> and Cl<sup>-</sup> and their  
 369 ratios (Cl<sup>-</sup>/Na<sup>+</sup>) in the TSP and PM<sub>1</sub> fractions.



370 **Figure 12.** Left panel: Time series of the elemental concentrations of Cl<sup>-</sup> and Na<sup>+</sup> in the TSP and PM<sub>1</sub>  
 371 fractions. Right panel: Time series of elemental ratio of Cl<sup>-</sup>/Na<sup>+</sup> in the TSP and PM<sub>1</sub> fractions. The grey  
 372 panels represent the different meteorological periods.

373

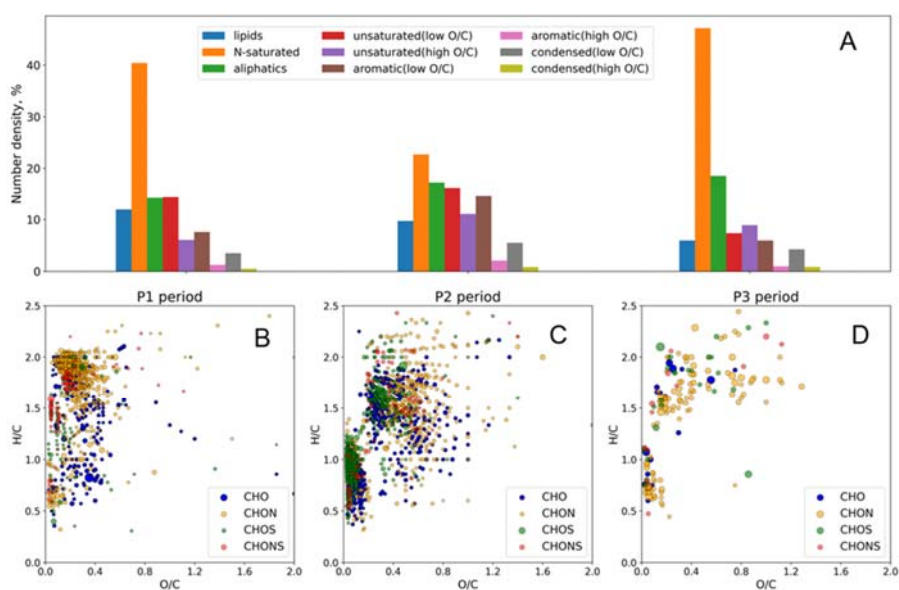
374 The concentrations of Na<sup>+</sup> and Cl<sup>-</sup>, strongly correlated as expected, showed a relatively  
 375 constant background of approximately 10 µg m<sup>-3</sup> (TSP) and 0.3 µg m<sup>-3</sup> (PM<sub>1</sub>), and intense  
 376 peaks of concentrations. In the TSP fraction, the Cl<sup>-</sup> concentration was up to 80 µg m<sup>-3</sup>. The  
 377 Cl<sup>-</sup>/Na<sup>+</sup> ratio was of the order of 1.5 in the P1 and P2 periods, and of the order of 1.8 afterwards.  
 378 In the PM<sub>1</sub> fraction, the Cl<sup>-</sup> concentration reached 2.5 µg m<sup>-3</sup>. The Cl<sup>-</sup>/Na<sup>+</sup> ratio, little  
 379 documented during P1, was around 0.7, while it increased between 1 and 1.8 during P2 and  
 380 P3. Values of the order of 1.5-1.8 are consistent with the composition of local seawater (Giorio  
 381 et al., this issue) and average sea spray (Seinfeld and Pandis, 2006), as well as the previous  
 382 results by Klopper et al. (2020).

Mis en forme : Centré  
 Tableau mis en forme

383

384 Both in the TSP and PM<sub>1</sub> fractions, the mass concentration of organic carbon (OC) through  
385 the campaign was strongly associated with Na<sup>+</sup> as well as Cl<sup>-</sup> (not shown). In the TSP fraction,  
386 where sufficient concentration allowed for robust measurements, the OC/Na<sup>+</sup> ratio was  
387 variable and ranged between 0.07 and 0.3, consistent with values reported by Frossard et al.  
388 (2014) for marine aerosol types. The molecular analysis of the organic composition provides  
389 insights into the sources affecting the OC/Na<sup>+</sup> ratio during the campaign (Figure 23).

Mis en forme : Indice



390

391 **Figure 23.** Population density of all molecular compositions based on Alcon classes (a), and van  
392 Krevelen diagrams for only unique molecular assignments in samples under study in the three periods  
393 (b-d), where unique formulae were determined only in a sample from the designated period. The size of  
394 the points reflects relative intensities in the mass spectra (not used in the analysis).

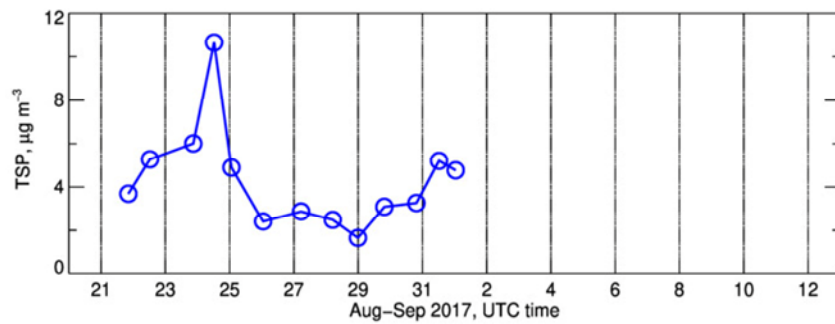
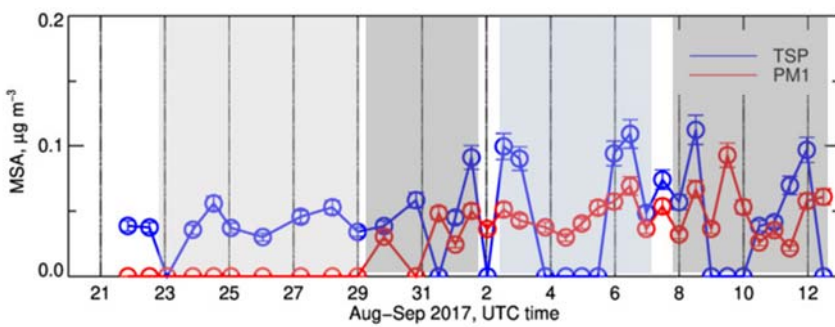
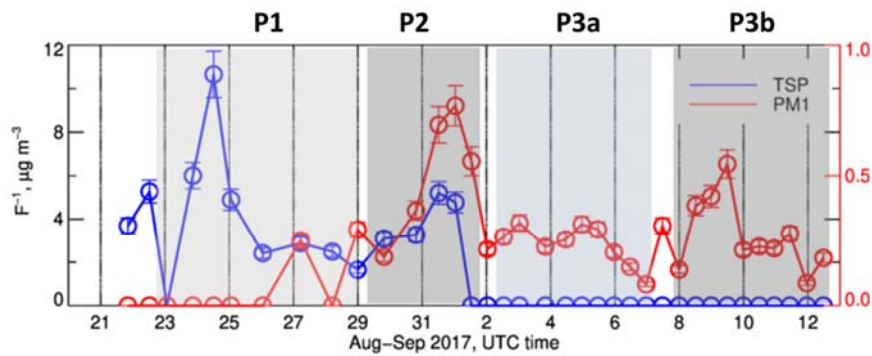
395

396 The differences in the molecular composition of samples from the P1-P3 periods are depicted  
397 in the van Krevelen diagrams (Figure 23b-d), which highlight the unique molecular  
398 composition of each period. P1 was dominated by saturated and low oxidized ( $O/C < 0.3$ ) CHO  
399 and CHON compounds, which occupy about 60% of the total molecular space (Figure 23).  
400 This may indicate the high contribution of biogenic fatty acids and protein-derived compounds  
401 (Bikkina et al., 2019). Their cumulative contribution in P2 decreased to about 40%, while a  
402 significant increase in the contribution of oxidized saturated compounds ( $O/C > 0.3$ ) as well as  
403 highly unsaturated ( $Al_{con} > 0.5$ ) compounds was observed. Moreover, reduced (low  $O/C$ )  
404 saturated compounds appear to be unique for the P1 period (Figure 23b). This supports the

405 biogenic source brought by south-westerly winds. Further, the contribution of continental dust  
406 with clear anthropogenic contribution is reflected as unique highly unsaturated compounds in  
407 the P2 period as well as an increase in S-containing compounds (Figure 2e3c). P3 was  
408 depleted with highly unsaturated compounds with a relative dominance of saturated N-  
409 containing compounds. The aerosol sources are similar between the P2 and P3 periods, which  
410 resulted in an insignificant amount of unique molecular assignment in the latter (Figure 2e3d).  
411 In addition, the double bond equivalent vs. molecular mass diagram in the supplementary  
412 material indicates an increase in the contribution of biomass-burning aerosols and possibly  
413 sulphate-enriched dust from smelting in the P2-P3 periods compared to the P1 period, which  
414 is in line with the air mass origin. Further details of the organic composition are reported in the  
415 supplementary materials.

### 416 3.2.2 Fluoride and MSA concentrations

417 The P1 and P2 periods were also characterised by extremely high concentrations of fluoride  
418 (up to  $10 \mu\text{g m}^{-3}$ ) as shown in Figure 34, in line with what reported by Klopper et al. (2020) for  
419 the  $\text{PM}_{10}$  aerosols measured during 2016 and 2017 at the site. In September (P3a and P3b),  
420 the concentration of  $\text{F}^-$  dropped to zero, as a consequence of the change in the origin of the  
421 air masses transported to the site.



422

423

424 **Figure 34.** Time series of the elemental concentrations of  $F^-$  and  $MSA$  in the TSP (top) and  $PM_{10}$  (bottom) fractions during the field campaign. Missing data correspond to periods when the measured concentrations were below the detection limits.

427

428 Fluoride is a natural occurring ion in marine environments as well as in mineral dust (Fuge, 2019). In Namibia, the release of dissolved fluoride to the atmosphere is due to the evaporation of fluoride-rich groundwater (Sracek et al., 2015) or the erosion of mineral deposits of calcium

Mis en forme : Centré

Mis en forme : Indice

Mis en forme : Normal (Web)

431 fluoride (CaF<sub>2</sub>, Onipe et al., 2020). Fluoride is present in significant amounts (> 1 wt.% F) in  
 432 francolite, a carbonate fluorapatite mineral (typical formula  
 433 Ca<sub>4.7</sub>Na<sub>0.2</sub>Mg<sub>0.1</sub>(PO<sub>4</sub>)<sub>2.6</sub>(CO<sub>3</sub>)<sub>0.4</sub>F<sub>1.28</sub>), which can be found in phosphorite deposits on the  
 434 Namibian shelf, notably in the area between 23° and 25.5°S south of Henties Bay (Compton  
 435 and Bergh, 2016; Mänd et al., 2018). This ~~is likely could to~~ be the origin of the excessive  
 436 fluoride concentrations observed during the P1 period of the campaign. Atlas and Pytkowicz  
 437 (1977) and Hossein et al (2024) describe the mechanism by which F<sup>-</sup> could be released in sea  
 438 water by dissolution. Upon dissolution, the release of F<sup>-</sup> to the atmosphere can be attributed  
 439 to the reaction with hydrogen in water to form hydrogen fluoride gas (or a solution of  
 440 hydrofluoric acid; Anbar, M., and Neta, 1967). The high content of fluoride in the Namibian soil  
 441 is also documented and attributed to weathering and dissolution of fluoride-containing minerals  
 442 (Hossein et al, 2024). Not only the origin of air masses detected at Henties Bay coincided with  
 443 the locations of the marine deposits, but during P1 the fluoride content correlated with major  
 444 marine tracers (Na, Cl, S; correlation coefficients R<sup>2</sup> = 0.87, 0.85 and 0.75, respectively), and  
 445 with calcium, both its sea salt and non-sea-salt fractions (nss-Ca<sup>2+</sup>/F<sup>-</sup> ratio ranging from 0.1 to  
 446 0.3, as in Klopper et al. (2020), correlation coefficients R<sup>2</sup> = 0.67 with nss-Ca<sup>2+</sup> and 0.79 with  
 447 Ca<sup>2+</sup>), as well as with P, K and Sr (correlation coefficients R<sup>2</sup> = 0.68, 0.91 and 0.21,  
 448 respectively), the latter can replace Ca in the francolite mineral structure (Compton and Bergh,  
 449 2016; Rakovan and Hughes, 2000). Note that, despite its high concentrations, fluoride was not  
 450 included in the source apportionment because it was not measured during the whole field  
 451 campaign.

452 The concentrations of methanesulfonic acid (MSA), tracer of marine biogenic productivity,  
 453 averaged at 61 ± 26 ng m<sup>-3</sup> in the TSP fraction and 46 ± 26 ng m<sup>-3</sup> in the PM<sub>10</sub> fraction. These  
 454 values are consistent with the yearly average in the PM<sub>10</sub> reported by Klopper et al. (2020).  
 455 While concentrations of F<sup>-</sup> and MSA appear unrelated in the TSP fraction, they remain above  
 456 detection limit in the PM<sub>10</sub> fraction, where they were measured starting from the P2 period only.  
 457 While the F<sup>-</sup> concentrations showed a certain degree of variability, the MSA remained constant  
 458 with time.

### 460 3.2.3 Mineral dust composition

461 Figure 4-5 presents the time series of the elemental concentrations of Al, Si and Fe, major  
 462 tracers of mineral dust, as well as of their ratios (Si/Al, Fe/Al and Fe/Si) in the TSP and PM<sub>10</sub>  
 463 fractions.

Mis en forme : Couleur de police : Automatique

Mis en forme : Couleur de police : Automatique, Exposant

Mis en forme : Couleur de police : Automatique

Mis en forme : Exposant

Mis en forme : Exposant

Mis en forme : Police : (Par défaut) Arial

Mis en forme : Non Surlignage

Mis en forme : Non Surlignage

Mis en forme : Non Exposant/ Indice, Non Surlignage

Mis en forme : Non Surlignage

Mis en forme : Indice, Non Surlignage

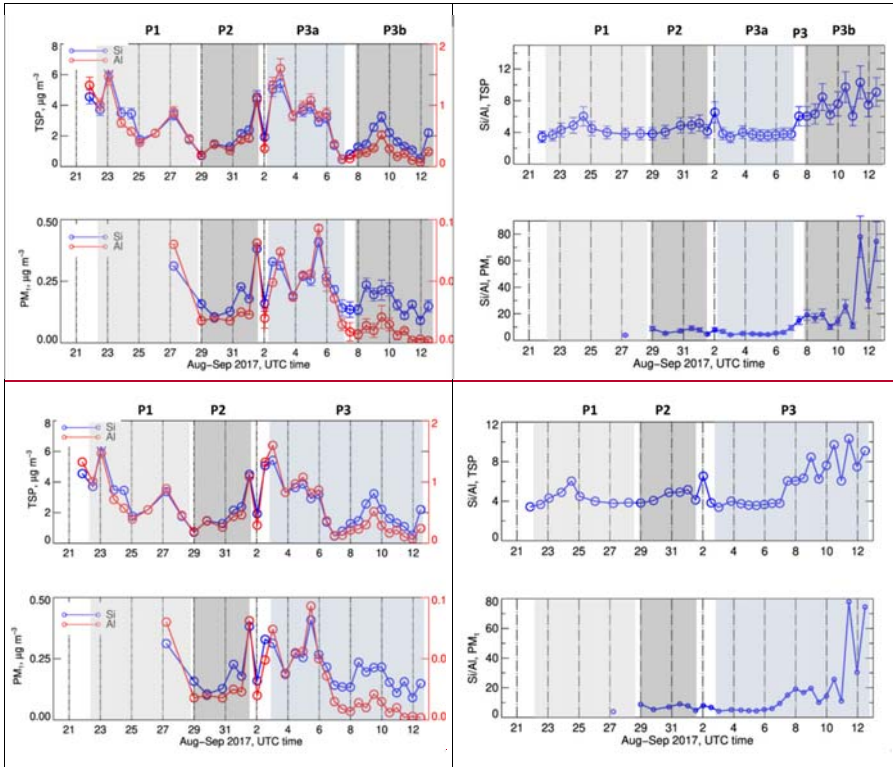
Mis en forme : Non Exposant/ Indice, Non Surlignage

Mis en forme : Non Surlignage

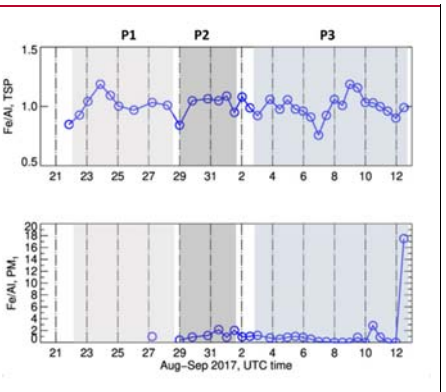
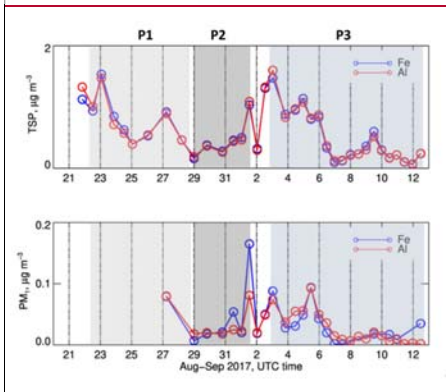
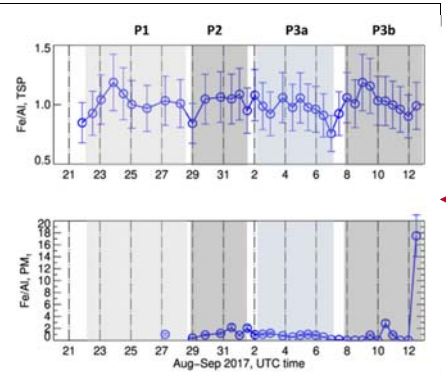
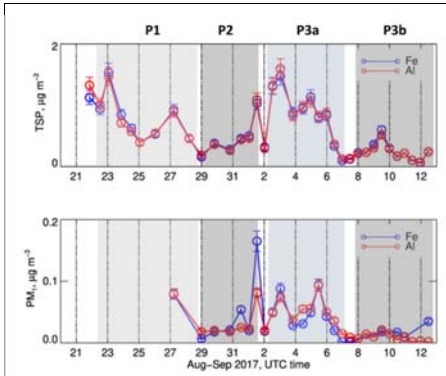
Mis en forme : Exposant

Mis en forme : Indice

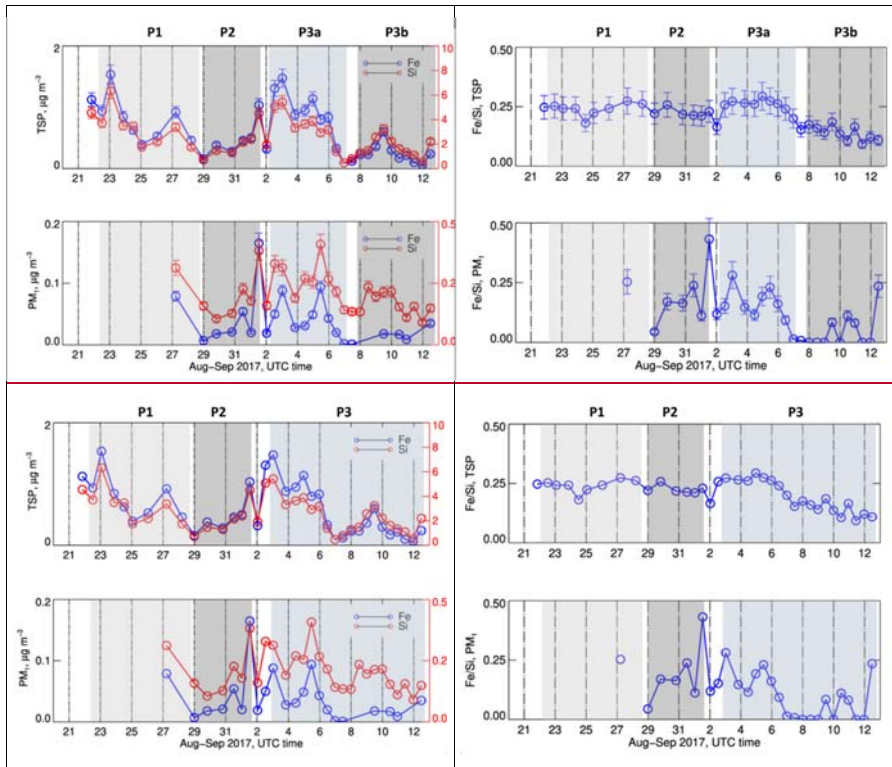
Mis en forme : Non Surlignage



Mis en forme : Centré  
 Tableau mis en forme



Mis en forme : Centré



464 **Figure 45.** Left panel, from top to bottom: Time series of the elemental concentrations Al, Si and Fe in the TSP and PM<sub>1</sub> fractions. Right panel from top to bottom: Time series of elemental ratio of Si/Al, Fe/Al  
 465 and Fe/Si in TSP and PM<sub>1</sub> fractions. Missing data correspond to periods when the measured  
 466 concentrations were below the detection limit.  
 467

468  
 469 The elemental concentrations of Si and Al were up to 6 and 1  $\mu\text{g m}^{-3}$  in the TSP fraction and  
 470 up to 410 and 90  $\text{ng m}^{-3}$  in the PM<sub>1</sub> fraction, respectively. In the P1 and P2 periods, and with  
 471 the exception of a peak value on 26-24 August, the Si/Al ratio was of the order of 3.8, consistent  
 472 with the findings of Klopper et al. (2020) for natural mineral dust emitted from the Namibian  
 473 gravel plains. After this date, that is during P3, the Si/Al ratio increased to values  
 474 between 6 and 10 (TSP) and between 8 and 80 (PM<sub>1</sub>), indicating a very strong enrichment with  
 475 respect to the composition of the regional mineral dust.

476 In the TSP fraction, and regardless of the period, the Fe/Al ratio was in the range of 0.8-1.2,  
 477 as previously found for the natural gravel plain dust in the area (Eltayeb et al., 1993; Klopper  
 478 et al., 2020). Likewise, during P1 and P2 the Fe/Si ratio was consistent with those previous  
 479 observations for mineral dust, and so was the Fe/Ca ratio (not shown), found in the range 0.2-  
 480 0.8. However, during P3, the Fe/Si decreased from approximately 0.25 to 0.1, while the Fe/Ca

481 ratio increased to between 0.09-0.15 (not shown). In the PM<sub>1</sub> fraction, both the Fe/Al and the  
482 Fe/Si ratios were more variable with time (only the September period is documented). The  
483 Fe/Al ratio was of the order of 1 as in the TSP fraction, except on the last day of the campaign  
484 when the ratio reached 18. The Fe/Si was higher between 29 August and 6 September (e.g.,  
485 the P2 period), ranging from 0.2 to 0.4, and decreased to 0.1-0.2 in the last days of the  
486 campaign. That corresponded to the variability of several major elements and metals (K, Mg,  
487 Co, Cu, Nd, Ni, Sr, Cd, but Zn, As and Pb in particular), whose ratio with Al were significantly  
488 higher during the last days of the campaign (7-12 September, Figure S5). As for OC/Na<sup>+</sup>, the  
489 aerosol mineral composition of TSP during the P3 period could be split into two sub-periods  
490 before and after 6 September, with an enrichment in metals and OC at the end of the campaign.

#### 491 **3.2.4 Source apportionment**

492 These observations are reflected by the PMF analysis, described in Text S2 in the  
493 supplementary material. Note that, despite its high concentrations, fluoride was not included  
494 in the source apportionment because it was not measured during the whole field campaign. In  
495 the TSP fraction, the analysis separates two factors characterized by a high loading of metals.  
496 The first one is a “mineral dust” factor characterized by Al, Fe, and Si, as well as Ti, Mn, Na<sup>+</sup>,  
497 Ca<sup>2+</sup>, and SO<sub>4</sub><sup>2-</sup>. Its contribution, significant only during the first part of the campaign,  
498 accounted, on average, for 5.8% of total TSP mass. The second factor, called “Si-rich”, is  
499 characterized by the presence of a high loading of Si, As and Pb, strongly correlated to each  
500 other (r=0.97), moderate loadings of Co, Cu, Ni, Nd, Sr, Zn and EC, but not correlated to Al  
501 nor Fe, contrarily to “mineral dust”. The “Si-rich” factor, significant mostly during the P3 period,  
502 notably after the 6 September, accounted for 23.3% of TSP mass but was not found in the PM<sub>1</sub>  
503 fraction where the concentrations of the majority of its tracers were very close to the detection  
504 limit. This is in agreement with the fact that the fraction of coarse particles with respect to the  
505 total number increased on the last days of the campaign (Figure S6 in the supplementary  
506 material).

507 The chemical fingerprinting of the “Si-rich” factor is similar to that reported from windblown dust  
508 from mines in the Otavi Mountainland in Namibia (Mileusnić et al., 2014; Sracek, 2015) as in  
509 the Zambian Copper Belt (Meter et al., 1999; Ettler et al., 2011; 2014; Mwaanga et al., 2019),  
510 a large and important mining area in the northern part of Zambia (Aurélien et al., 2022;  
511 Martinez-Alonso et al., 2023; Křibek et al., 2023). Sracek (2015) found various associations of  
512 Fe with Cu, Co, Pb, V, As, Pb, and Zn for mines in Zambia and Namibia, characterized by  
513 different climates and ages of the core. At a receptor site on the Zambian Copperbelt in  
514 Zimbabwe, the analysis by Nyanganyura et al. (2007) identified the mixing of mineral dust and  
515 metal smelting emissions by distinguishing the long-range transport of a aerosols containing  
516 Fe, Al, Si but also Co from a non-ferrous smelter component contributing to the fine aerosol

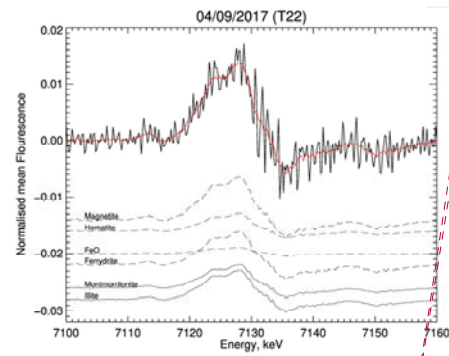
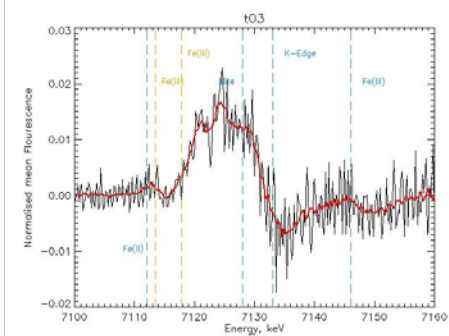
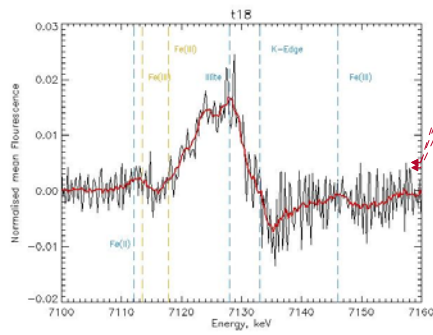
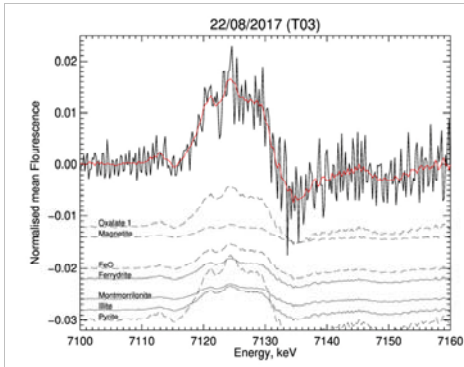
517 fraction only, and characterized by S, Zn, As, and Pb. Ettler et al. (2007) indicated that iron is  
518 enriched both with respect to Al and Si in dust liberated from Cu–Co metal smelters in the  
519 Zambian Copperbelt. However, Meter et al. (1999) showed that enrichment is variable on an  
520 event basis depending on the pyro-metallurgical processing of ores and their composition.

521 We henceforth conclude that during P1 and P2 the aerosol composition was dominated by  
522 natural Namibian mineral dust sources with a composition very similar to the average dust  
523 composition measured at the same site in 2016-2017 (Klopper et al., 2020) and reaching the  
524 site within the southerly air flow. Conversely, during the last part of P3, the dust reaching  
525 Henties Bay was fugitive material from anthropogenic activities. The air masses during the  
526 second part of P3 could originate as far as from the Zambian Copper belt.

527 These conclusions are further corroborated by the CAMS reanalysis shown in Figure S7 in the  
528 supplementary material. During P1 and P2 the dust mass mixing ratio reached up to  $120 \mu\text{g m}^{-3}$   
529 ( $100 \mu\text{g kg}^{-1}$  on the CAMS map) at the surface in correspondence with the coastal sources  
530 in Namibia as a response to the prevailing south-easterly winds (Figure S4S3) dominating the  
531 near-surface circulation from 23 August to 3 September. Continental dust sources were  
532 activated on 22 August and 1 September, in association with south-westerly near-surface  
533 winds, and on 28-29 August and 4-5 September, in association with near surface convergence  
534 of south-westerly and north-easterly winds. From 6 September onwards, no remarkable dust  
535 activity was observed, while the circulation had changed (Figure S7). The CAMS reanalysis  
536 also showed that the sulphate mixing ratios at the surface reached  $6 \mu\text{g m}^{-3}$  ( $5 \mu\text{g kg}^{-1}$  on the  
537 CAMS map) in the Zambian Copper Belt and in the urban area of Pretoria and Johannesburg  
538 (Figure S7), also a known pollution hotspot (Martinez-Alonso et al., 2023). Sulphate aerosols  
539 remained close to their source regions until the end P2. With the installation of the continental  
540 high on the 3 September, sulphate aerosols were recirculated south-westwards towards  
541 Henties Bay during P3, in particular during 10-12 September.

### 542 3.3 Iron mineralogy

543 The first derivative of the ~~four~~-XANES normalized spectra ~~corresponding for four samples~~  
544 ~~collected during the different periods of~~ ~~to the highest Fe concentrations measured during~~  
545 AEROCLO-sA are shown in Figure 56. The remaining spectra, including those of the standard  
546 minerals and compounds used for the deconvolution, are reported in Figure S8.



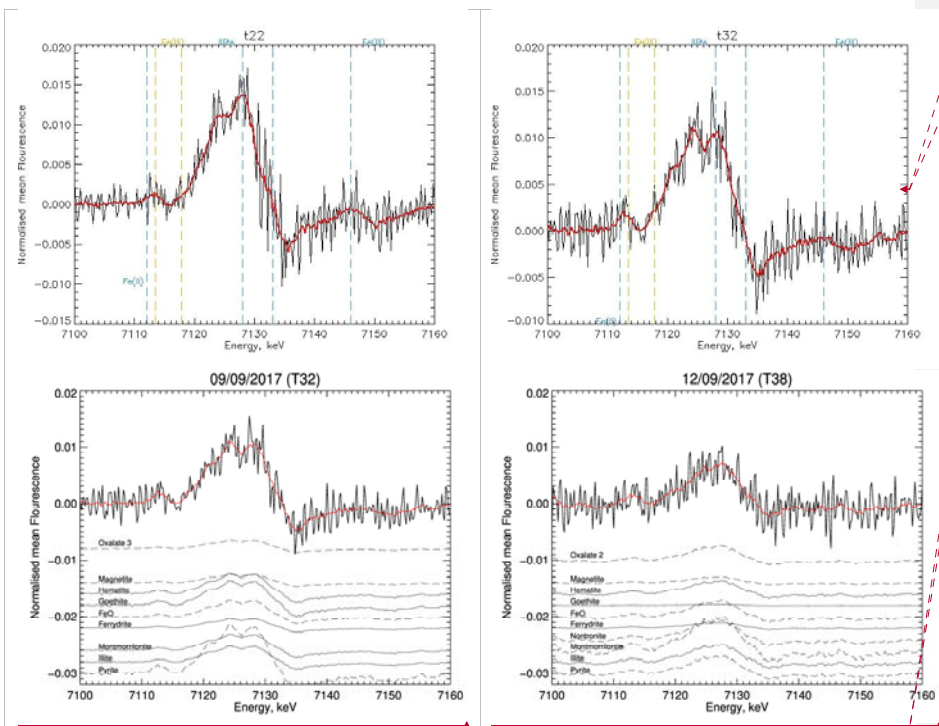
Mis en forme : Centré

Tableau mis en forme

Mis en forme : Normal (Web), Centré, Espace Avant : 0 pt, Interligne : simple

Mis en forme : Police :Français (France)

Mis en forme : Français (France)



Mis en forme : Normal (Web), Centré, Espace Avant : 0 pt, Interligne : simple

Mis en forme : Normal (Web), Gauche, Espace Avant : 0 pt, Interligne : simple

Mis en forme : Police :Français (France)

Mis en forme : Police :Français (France)

547 **Figure 56.** First derivative of the four XANES normalized (black lines) spectra corresponding to the  
 548 highest Fe concentrations measured during AEROCLO-sA (see Table S3). The spectral positions of the  
 549 absorption bands of Fe(II) and Fe(III) in the pre-edge region (7112.1 to 7117.8 eV) as well as those of  
 550 illite (7128 eV) and various Fe(III) minerals, including hematite (7146 eV), according to Wilke et al.  
 551 (2004) are indicated by vertical intermittent lines and corresponding to different periods and mineralogy.  
 552 The red lines correspond to the fitted spectra. The contribution of the individual standards to the total  
 553 measured signal is also reported. The dotted lines represent the contributions smaller than 10%, which  
 554 have been multiplied by a factor of 10 to ease their visualisation.

555

556 Because of the small quantities of particle mass collected on the filters, the XANES spectra  
 557 are rather noisy. The main features can nevertheless be explored after smoothing. They all  
 558 are rather similar. In the region between 7122 and 7128 eV, two to three peaks are present  
 559 with different intensities depending on the sample. The peak at 7128 eV is minor on sample  
 560 T03 (P1 period) for which the peaks at 7122 and 7126 eV dominate. The peak at 7122 eV is  
 561 not present afterwards. For samples T18 and T22 in the P2 and beginning of P3 periods, only  
 562 the peaks at 7126 and 7128 eV are present, the intensity of the latter being higher than the  
 563 one of the former, while those peaks have equal intensity on sample T032 in the P3 period.  
 564 For mineral dust from northern Africa, Formenti et al. (2014) showed that the relative  
 565 proportions of these peaks can be related to the type of clays, but also to the presence of iron  
 566 oxides in the form of hematite ( $\text{Fe}_2\text{O}_3$ ) or goethite ( $\text{FeOOH}$ ). Peaks between 7132 and 7136

567 eV are distinctive of clays and iron oxides in the form of hematite, but are not present for  
 568 goethite. In our samples, a minor shoulder in this spectral region is observed only for a few  
 569 samples (T24, T25, and T31) collected in September. On the other hand, the pre-edge region  
 570 between 7110 and 7116 eV is sensitive to the iron oxidation state. The majority of our samples  
 571 seem to peak around 7113-7114 eV, indicating that iron is predominantly in the Fe(III) oxidation  
 572 state. Only for a few samples (T10, T25, T26, T30, and T37), the pre-edge peak is closer to  
 573 7112 eV indicating that Fe(II) could be the predominant oxidation state.

574 Several attempts of least square reduction were done with a variable number of references to  
 575 reflect the many mineralogical forms in which iron can be found and verify the stability of the  
 576 solution. While the relative proportions might have changed by a few percent, the overall  
 577 repartition was found to be consistent and independent of the selected references.

578 The average least-square apportionment of the total TSP elemental iron is presented in Table  
 579 1 in terms of the mean fractions par sampling period and mineralogical classes.

580

581 **Table 1.** Apportionment of total iron (percent mean and standard deviation) by the least-square  
 582 deconvolution of the XANES spectra obtained on the filter samples indicated in the first row. Results are  
 583 grouped by period and by mineral classes.

	<b>21-31 Aug 2017 T01-T14</b>	<b>1-2 Sep 2017 T15-T18</b>	<b>2-7 Sep 2017 T20-T27</b>	<b>8-12 Sep 2017 T28-T38</b>
<b>Clays</b>	49 ± 13	58 ± 12	53 ± 11	42 ± 10
<b>GoethiteIron oxides</b>	<u>40-10 ± 104</u>	<u>936 ± 82</u>	<u>40-6 ± 95</u>	<u>6 ± 346 ± 8</u>
<b>Hematite</b>	<u>7 ± 5</u>	<u>8 ± 7</u>	<u>15 ± 11</u>	<u>9 ± 7</u>
<b>Magnetite</b>	<u>10 ± 5</u>	<u>9 ± 8</u>	<u>15 ± 11</u>	<u>14 ± 6</u>
<b>Oxalate</b>	4 ± 4	3 ± 4	3 ± 4	5 ± 7
<b>Pyrite</b>	7 ± 5	3 ± 4	4 ± 5	7 ± 4
<b>Ferrihydrite</b>	<u>17 ± 7</u>	<u>14 ± 12</u>	<u>8 ± 4</u>	<u>16 ± 4</u>

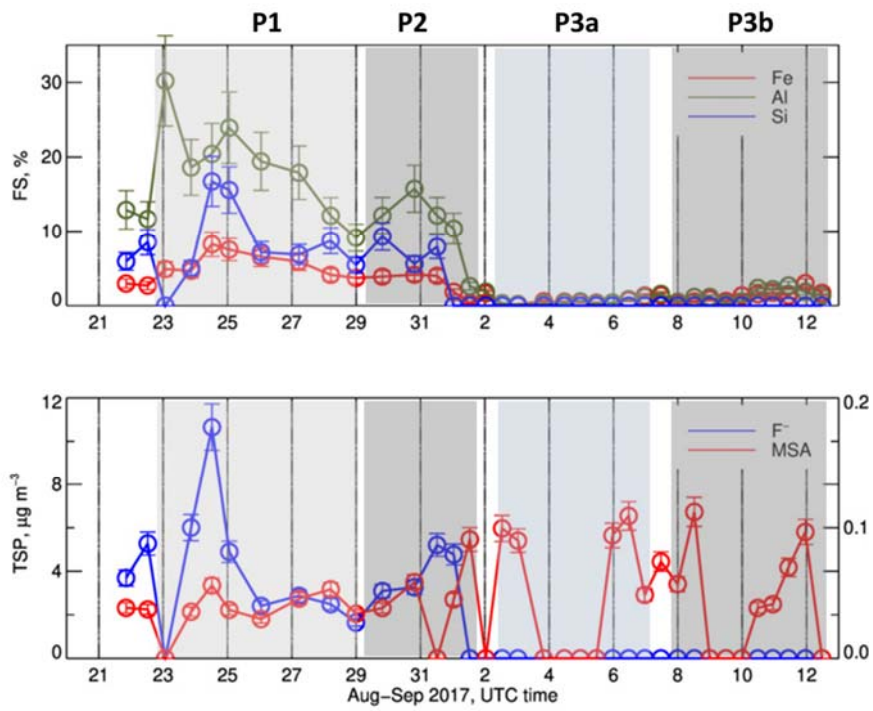
584

585 The largest contribution to the total iron is by clays, between 42 to 58%, with illite and  
 586 montmorillonite contributing in equal proportions. While a clear temporal trend cannot be  
 587 defined, the contribution of clays is lowest during the latest sampling period (6-12 September  
 588 2017). The second largest contribution is by iron oxides, accounting for between 38 to 45% of  
 589 the total iron throughout the sampling period. The contribution of FeO, iron oxide in Fe(II) form,  
 590 is low and extremely variable from sample to sample and not necessarily retrieved for samples  
 591 in which a shift towards the Fe(II) seems evident in the pre-edge region (T10, T25, T26, T30,  
 592 and T37). The period P3 is also characterized by the lowest contribution of Fe(III) oxide (64%  
 593 vs 72-75%). Ferrihydrite (14 ± 7% of total iron) and goethite (8 ± 6% of total iron) showed their  
 594 highest contributions during P2 (21% and 12% respectively), while hematite (8 ± 6 of total iron)  
 595 was highest in September (P3). Sracek (2015) found that the formation of secondary hematite

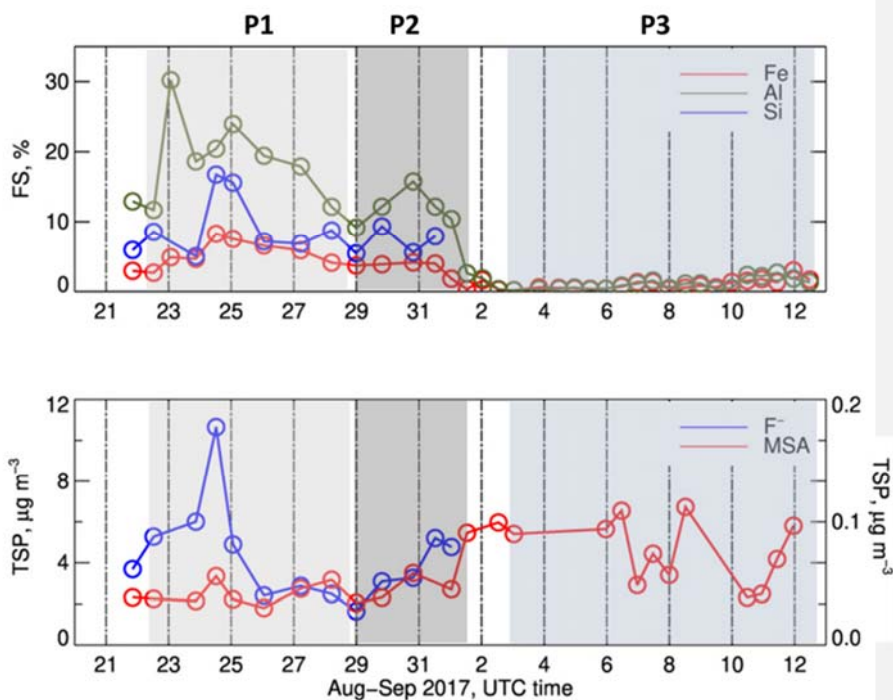
596 is favoured by tropical climate conditions in mines in Zambia compared to Namibia. In contrast  
597 to northern African dust, the least-square reduction shows that the presence of magnetite is  
598 significant in the dust collected during the campaign, contributing 10-15% to the total iron oxide  
599 fraction. Magnetite can be found in sediments in the Erongo region of coastal Namibia  
600 (Lohmeier et al. 2021), but also in anthropogenic emissions, such as for example those from  
601 metal smelting (Rathod et al. 2020). Zhang et al. (2022) investigated the light-absorbing  
602 properties and single particle composition from airborne measurements offshore central Africa  
603 during the ORACLES 2018 campaign, and attributed the presence of magnetite to the high-  
604 temperature conversion of hematite and/or goethite in biomass-burning plumes or to industrial  
605 or vehicular emissions, including from pyro-metallurgical processing in the Zambian  
606 Copperbelt. Pyrite (FeS) and Fe-oxalate complexes were also detected throughout the  
607 campaign, by their average contribution was extremely low, with the exceptions of 28-29  
608 August 2017 (T10, approximately 19%) and 11 September (T35-36, approximately 30%).

#### 609 **3.4 Iron solubility**

610 Figure 6-7 presents the time series of the fractional solubility for Al, Si and Fe, as well as those  
611 of fluoride (F<sup>-</sup>) and MSA measured in the TSP fraction during the field campaign.



612



613  
 614 **Figure 76.** Top panel: Time series of the fractional solubility Al, Si and Fe in the TSP fraction. Bottom  
 615 panel: Time series of concentrations of F<sup>-</sup> (blue) and MSA (red) in the TSP fraction. The MSA  
 616 concentrations are reported on the right axis of lower panel. Missing data correspond to periods when  
 617 the measured concentrations were below the detection limit.

618  
 619 During P1 and P2, the fractional solubility was measurable and of the order of 2-8% for Fe, 9-  
 620 24% for Al, 5-17% for Si and 1.5-4% for Ti (not shown). After that, during P3, their fractional  
 621 solubility drastically dropped to 0.2-1.7% for Fe and 0.2-2.6% for Al, whereas the fractional  
 622 solubility of Si and Ti was not measurable (dissolved concentrations under limit of detection).  
 623 A similar behaviour was observed for most of the measured trace metals (As, Co, Cr, Cu, Ni,  
 624 Pb, Ti, and Zn, Figure S9).

625 The percent fractional solubility of iron measured during P1 and P2 was of the same order of  
 626 magnitude as the lowest solubility values reported at the same sampling site for PM<sub>10</sub> dust  
 627 particles by Desboeufs et al. (2024) for the period April to December 2017, when values as  
 628 high as 20% were measured when MSA in the particle phase was most concentrated. These  
 629 authors attributed the enhanced solubility to processing (photo-reduction) of the dust by gas-  
 630 phase dimethyl sulphide (DMS) emitted by the coastal Benguela upwelling. In the present  
 631 dataset, this association cannot be made. Figure 76 shows that the MSA concentrations were

632 of the same order of magnitude throughout the campaign, and actually slightly more  
633 concentrated during P2 and P3, when, on the other hand, the Fe fractional solubility was the  
634 lowest. Soluble Fe was also not correlated with oxalate (Pearson correlation coefficient  $r \sim$   
635 0.3), another renowned organic ligands (Paris and Desboeufs, 2013).

636 On the other hand, Figure 6-7 shows that during P1 and P2, the temporal variability of the  
637 fractional solubility of Al, Si and Fe closely followed that of the mass concentration of fluoride  
638 (correlation coefficient of 0.87, 0.85 and 0.81, respectively). Fluoride has been identified to be  
639 a good ligand of metals in aqueous solution, notably Fe(III) in comparison to Fe(II) (Connick et  
640 al., 1956; Bond and Hefter, 1980). The abundance of fluoride ions could act to facilitate the  
641 metal complexation on the particle surfaces, potentially promoting their release from the bulk  
642 oxide and dissolution at the solid/liquid interface (Arnesen et al., 1998; Tao et al., 2022). In  
643 particular,  $F^-$  may contribute to the disruption of the Si-O lattice bond by forming  $SiF_6^{2-}$   
644 complexes at acidic pH (Mitra and Rimstidt, 2009).

#### 645 **4 Conclusive remarks**

646 The three weeks of aerosol sampling at the Henties Bay coastal site in Namibia during the  
647 AEROCLO-sA field campaign coincided with a transition period between two synoptic regimes:  
648 the dominance of southerly air flow, associated with the reinforcement of the South Atlantic  
649 anticyclone (22 to 31 August 2017) and the dominance of north-easterly air flow (1 to 12  
650 September 2017), associated with the installation of the mid-tropospheric continental high.  
651 Those synoptic regimes corresponded to a significant change in the aerosol composition  
652 measured at the site and in particular of that of mineral dust. During August and the first few  
653 days of September, the dust was natural windblown from the southerly gravel plains with a  
654 composition consistent with that previously found in Namibia (Klopper et al., 2020). ~~Gate~~Later,  
655 the dust was fugitive from anthropogenic mining and possibly also from smelting emissions as  
656 far as in the Zambian Copper Belt. The anthropogenic influence in the latter part of the  
657 campaign was also documented by the composition of the organic aerosol, which was rich in  
658 highly unsaturated compounds as well as saturated N-containing compounds in the latter two  
659 periods, more typical of anthropogenic pollution. A second major difference in the composition  
660 of the air masses was the high fluoride content until September 2 attributed to emissions from  
661 the marine shelf south of Henties Bay.

662 Taking advantage of those differences, this paper presents the first case study analysis of  
663 differences and similarities in the composition of natural and anthropogenic dust, with two key  
664 findings: (1) the elemental composition of the anthropogenic dust is enriched in silicon and  
665 heavy metals, notably As, Mn, Cu, Cd, Pb, and Zn, and depleted in Al; (2) metals in  
666 anthropogenic dust are less water-soluble than in the natural aeolian dust. In particular, the

667 fractional solubility of iron in the natural dust ranged between 2 and 8%, but remained lower  
668 than 2% in the anthropogenic dust. This is rather unexpected when taking into account the  
669 current literature on anthropogenic dust influenced by combustion, reporting that the iron  
670 solubility would be the order of 50% (e.g., Li et al., 2017; Ueda et al., 2023). There are various  
671 possible explanations to this fact. First of all, the mineralogy of iron. The most soluble form,  
672 ferrihydrite (Journet et al., 2008; Shi et al., 2012), was slightly more abundant in the natural  
673 dust, while the less soluble forms of iron (iron oxides such as hematite and magnetite) were  
674 more frequent in the fugitive dust, which conversely, could be more efficient in absorbing light  
675 at short wavelengths. Secondly, during the first part of the campaign, the aerosol particles were  
676 smaller in size, which is known to promote particle solubility, both directly but also in an indirect  
677 way, allowing more intense atmospheric processing (Hamilton et al., 2022). Thirdly, our results  
678 indicate in a very clear way the extent of which the solubility of iron is linked to the abundance  
679 of fluoride ions during the first part of the campaign. While we do not have insights in the  
680 mineralogical forms of the metals other than iron, the similar behaviour of their dissolved  
681 concentrations, in particular Al and Si, suggest that the marine emissions of fluoride from the  
682 Benguela shelf could play a key role in sustaining the complexation of metals dust particles  
683 and facilitate their dissolution, supplementing the processing by DMS described for iron in  
684 Desboeufs et al. (2024). Such high concentrations of F<sup>-</sup> ions are not only unexpected but also  
685 they open questions for further studies in this environment. Similarly, to what is known for  
686 chloride or bromine (Finlayson-Pitts, 2010, Simpson et al., 2015) one cannot exclude recycling  
687 F<sup>-</sup> into reactive fluorinated radicals through heterogeneous processes. This call for further  
688 targeted reanalysis of the organic matter sampled during this campaign both the gaseous and  
689 particulate phases and for further laboratory work to investigate this quite poorly know  
690 chemistry. Finally, our results suggest that, in the absence of processing by DMS or oceanic  
691 fluoride, the transport of mining dust, including from the Zambian Copper Belt, is unlikely to be  
692 a significant source of dissolved iron, but also of elements such as Mn, Cu and Zn, which are  
693 toxic to phytoplankton even at low concentrations, and if assimilated, could alter the oceanic  
694 productivity and microbial biogeochemistry (Adriano, 2001; Jordi et al., 2012; Mahowald et al.,  
695 2018; Yang et al. 2019).

696 Future work should expand these results by addressing the frequency and intensity of those  
697 occurrences on a longer time scale, as well as the mineralogy of metals and their processing  
698 by marine emissions in the laboratory.

699

700 **Data Availability.** All data are made freely available by the French national service for  
701 atmospheric data AERIS at <https://pegasus.aeris-data.fr/catalogue/>. All data are made freely  
702 available by the French national service for atmospheric data AERIS SEDOO data at  
703 <https://baobab.sedoo.fr/AEROCLO/>.

704 **Code Availability.** The FASTOSH XANES data analysis package is available for download at  
705 <https://www.synchrotron-soleil.fr/fr/lignes-de-lumiere/samba> (last accessed: 02/03/2024).

706 **Author contribution.** PF coordinated the AEROCLO-sA project and funding, led the field  
707 campaign and the data analysis, and wrote the manuscript with contributions from all the co-  
708 authors. SM performed PMF analysis. AZ performed ESI-HRMS analysis and analysed data.  
709 CG collected samples, supervised PMF and ESI-HRMS analyses and their data interpretation.  
710 CB contributed to the interpretation of the dust solubility and composition. KD analysed the  
711 fractional solubility measurements. MG analysed CAMS reanalysis. GS performed back-  
712 trajectories calculations. SC performed XRF analysis, ST performed IC / ICP analysis, FB and  
713 CDB performed XANES measurements under the supervision of GL. AF, JFD, AN and SJP  
714 participated and facilitated the field campaign.

715 **Special issue statement.** This article is part of the special issue “New observations and  
716 related modelling studies of the aerosol–cloud–climate system in the Southeast Atlantic and  
717 southern Africa regions (ACP/AMT inter-journal SI)”. It is not associated with a conference.

718 **Competing interests.** Some authors are members of the editorial board of journal ACP.

#### 719 **Acknowledgements**

720 Authors are grateful to the AEROCLO-sA consortium for their work in the field and during the  
721 preparation of the field campaign, and SANUMARC for hosting the field campaign. The authors  
722 wish to thank AERIS (<https://www.aeris-data.fr/>), the French center for atmospheric data and  
723 service, for providing the campaign website and organizing the curation and open distribution  
724 of AEROCLO-sA data.

#### 725 **Funding support**

726 This work was supported by the French National Research Agency under grant agreement n°  
727 ANR-15-CE01-0014-01, the French national program LEFE/INSU, the French National Agency  
728 for Space Studies (CNES), and the South African National Research Foundation (NRF) under  
729 grant UID 105958. CG’s work was supported by the Supporting TAlent in  
730 ReSearch@University of Padova STARS-StG “MOCAA”, and a BP Next Generation fellowship  
731 awarded by the Yusuf Hamied Department of Chemistry at the University of Cambridge. This  
732 research received additional resources through the “The role of Secondary Organic Aerosols  
733 on the climate over the west coast of southern Africa (SOA-Clim)”, International Research  
734 Project supported by University of Cambridge and CNRS. MG was supported by the project  
735 “Dipartimento di Eccellenza 2023–2027”, funded by the Italian Ministry of Education, University  
736 and Research at IUSS Pavia. The PEGASUS facility receives funding as a national facility  
737 (instrument national) of the CNRS INSU.

738 **References**

- 739 Adebisi, A., Kok, J. F., Murray, B. J., Ryder, C. L., Stuut, J.-B. W., Kahn, R. A., Knippertz, P.,  
740 Formenti, P., Mahowald, N. M., Pérez García-Pando, C., Klose, M., Ansmann, A., Samset, B.  
741 H., Ito, A., Balkanski, Y., Di Biagio, C., Romanias, M. N., Huang, Y., and Meng, J.: A review of  
742 coarse mineral dust in the Earth system, *Aeol. Res.*, 60, 100849,  
743 <https://doi.org/10.1016/j.aeolia.2022.100849>, 2023.
- 744 Adriano, D.C., Trace elements in terrestrial environments: biogeochemistry, bioavailability, and  
745 risks of metals. 2nd ed. New York Berlin Heidelberg: Springer, <https://doi.org/10.1007/978-0->  
746 387-21510-5, 2001.
- 747 [Anbar, M., and Neta, P.: Reaction of fluoride ions with hydrogen atoms in aqueous solution,](#)  
748 [Transactions of the Faraday Society, 63, 141-146, 10.1039/TF9676300141, 1967.](#)
- 749 Arnesen, A. K. M.: Effect of fluoride pollution on pH and solubility of Al, Fe, Ca, Mg, K and  
750 organic matter in soil from Ardal (Western Norway), *Water, Air, Soil Pollut.*, 103(1–4), 375–  
751 388, doi:10.1023/A:1004921600022, 1998.
- 752 [Atlas, E., and Pytkowicz, R. M.: Solubility behavior of apatites in seawater, Limnology and](#)  
753 [Oceanography, 22, 290-300, https://doi.org/10.4319/lo.1977.22.2.0290, 1977.](#)
- 754 Aurélien, N. , Ousmane, S. and Pitiya, R., Zambia's Copperbelt Area and Copper Mining: A  
755 Review. *J. Geosci. Environ. Protection*, 10, 67-75. doi: 10.4236/gep.2022.103005, 2022.
- 756 Bikkina, P., Kawamura, K., Bikkina, S., Kunwar, B., Tanaka, K., and Suzuki, K.: Hydroxy Fatty  
757 Acids in Remote Marine Aerosols over the Pacific Ocean: Impact of Biological Activity and  
758 Wind Speed, *ACS Earth and Space Chemistry*, 3, 366-379,  
759 10.1021/acsearthspacechem.8b00161, 2019.
- 760 Bond, A. M. And Hefter, G. T. (Eds.): Critical Survey of Stability Constants and Related  
761 Thermodynamic Data of Fluoride Complexes in Aqueous Solution, Pergamon, ii,  
762 <https://doi.org/10.1016/B978-0-08-022377-3.50001-6>, 1980.
- 763 Caponi, L., Formenti, P., Massabó, D., Di Biagio, C., Cazaunau, M., Pangui, E., Chevaillier,  
764 S., Landrot, G., Andreae, M. O., Kandler, K., Piketh, S., Saeed, T., Seibert, D., Williams, E.,  
765 Balkanski, Y., Prati, P., and Doussin, J.-F.: Spectral- and size-resolved mass absorption  
766 efficiency of mineral dust aerosols in the shortwave spectrum: a simulation chamber study,  
767 *Atmos. Chem. Phys.*, 17, 7175-7191, <https://doi.org/10.5194/acp-17-7175-2017>, 2017.
- 768 Cavalli, F., Viana, M., Yttri, K. E., Genberg, J. and Putaud, J.-P.: Toward a standardised  
769 thermal-optical protocol for measuring atmospheric organic and elemental carbon: the  
770 EUSAAR protocol, *Atmos. Meas. Tech.*, 3(1), 79–89, doi:10.5194/amt-3-79-2010, 2010.
- 771 [Chen, S., Chen, J., Zhang, Y., Lin, J., Bi, H., Song, H., Chen, Y., Lian, L., Liu, C., and Zhang,](#)  
772 [R.: Anthropogenic dust: sources, characteristics and emissions, Environmental Research](#)  
773 [Letters, 18, 103002, 10.1088/1748-9326/acf479, 2023.](#)
- 774 Compton, J. S., and Bergh, E. W.: Phosphorite deposits on the Namibian shelf, *Marine*  
775 *Geology*, 380, 290-314, <https://doi.org/10.1016/j.margeo.2016.04.006>, 2016.
- 776 Connick, R. E., Hepler, L. G., Hugus, Z. Z. Jr., Kury, J. W., Latimer, W. M., and Tsao, M.-S.:  
777 The Complexing of Iron(III) by Fluoride Ions in Aqueous Solution: Free Energies, Heats and  
778 Entropies, *J. Am. Chem. Soc.*, 78, 1827–1829, <https://doi.org/10.1021/ja01590a015>, 1956.
- 779 Desboeufs, K., Formenti, P., Torres-Sánchez, R., Schepanski, K., Chaboureaud, J.-P.,  
780 Andersen, H., Cermak, J., Feuerstein, S., Laurent, B., Klopfer, D., Namwoonde, A.,  
781 Cazaunau, M., Chevaillier, S., Feron, A., Mirande-Bret, C., Triquet, S., and Piketh, S. J.:  
782 Fractional solubility of iron in mineral dust aerosols over coastal Namibia: a link to marine  
783 biogenic emissions?, *Atmos. Chem. Phys.*, 24, 1525–1541, <https://doi.org/10.5194/acp-24->  
784 1525-2024, 2024.

785 Ettler, V., Mihaljevič, M., Kříbek, B., Majer, V., and Šebek, O.: Tracing the spatial distribution  
786 and mobility of metal/metalloid contaminants in Oxisols in the vicinity of the Nkana copper  
787 smelter, Copperbelt province, Zambia, *Geoderma*, 164, 73-84,  
788 <https://doi.org/10.1016/j.geoderma.2011.05.014>, 2011.

789 Ettler, V., Vítková, M., Mihaljevič, M., Šebek, O., Klementová, M., Veselovský, F., Vybíral, P.,  
790 and Kříbek, B.: Dust from Zambian smelters: mineralogy and contaminant bioaccessibility,  
791 *Environmental Geochemistry and Health*, 36, 919-933, [10.1007/s10653-014-9609-4](https://doi.org/10.1007/s10653-014-9609-4), 2014.

792 Finlayson-Pitts, B., Halogens in the troposphere, *Anal. Chem.*, 82, 3, 770–776,  
793 <https://doi.org/10.1021/ac901478p>, 2010.

794 Flamant, C., Gaetani, M., Chaboureaud, J.-P., Chazette, P., Cuesta, J., Piketh, S. J., and  
795 Formenti, P.: Smoke in the river: an Aerosols, Radiation and Clouds in southern Africa  
796 (AEROCLO-sA) case study, *Atmos. Chem. Phys.*, 22, 5701–5724, [https://doi.org/10.5194/acp-](https://doi.org/10.5194/acp-22-5701-2022)  
797 [22-5701-2022](https://doi.org/10.5194/acp-22-5701-2022), 2022.

798 Formenti, P., S. Nava, P. Prati, S. Chevaillier, A. Klaver, S. Lafon, F. Mazzei, G. Calzolari, and  
799 M. Chiari, Self-attenuation artifacts and correction factors of light element measurements by  
800 X-ray analysis: Implication for mineral dust composition studies, *J. Geophys. Res.*, 115,  
801 D01203, [doi:10.1029/2009JD012701](https://doi.org/10.1029/2009JD012701), 2010.

802 Formenti, P., S. Caquineau, S. Chevaillier, A. Klaver, K. Desboeufs, J. L. Rajot, S. Belin and  
803 V. Briois, Dominance of goethite over hematite in iron oxides of mineral dust from Western  
804 Africa: quantitative partitioning by X-ray absorption spectroscopy, *J. Geophys. Res.*, 119,  
805 12740-1275, 2014.

806 Formenti, P., D'Anna, B., Flamant, C., Mallet, M., Piketh, S. J., Schepanski, K., Waquet, F.,  
807 Auriol, F., Brogniez, G., Burnet, F., Chaboureaud, J.-P., Chauvigné, A., Chazette, P., Denjean,  
808 C., Desboeufs, K., Doussin, J.-F., Elguindi, N., Feuerstein, S., Gaetani, M., Giorio, C., Klopper,  
809 D., Mallet, M. D., Nabat, P., Monod, A., Solmon, F., Namwoonde, A., Chikwililwa, C., Mushi,  
810 R., Welton, E. J. and Holben, B.: The Aerosols, Radiation and Clouds in Southern Africa Field  
811 Campaign in Namibia: Overview, Illustrative Observations, and Way Forward, *Bull. Am.*  
812 *Meteorol. Soc.*, 100(7), 1277–1298, [doi:10.1175/BAMS-D-17-0278.1](https://doi.org/10.1175/BAMS-D-17-0278.1), 2019.

813 Frossard, A. A., Russell, L. M., Burrows, S. M., Elliott, S. M., Bates, T. S., and Quinn, P. K.:  
814 Sources and composition of submicron organic mass in marine aerosol particles, *J. Geophys.*  
815 *Res.*, 119, 12,977-913,003, <https://doi.org/10.1002/2014JD021913>, 2014.

816 Fuge, R.: Fluorine in the environment, a review of its sources and geochemistry, *Appl.*  
817 *Geochemistry*, 100, 393–406, [doi:10.1016/j.apgeochem.2018.12.016](https://doi.org/10.1016/j.apgeochem.2018.12.016), 2019.

818 Gaetani, M., Pohl, B., Alvarez Castro, M. C., Flamant, C., and Formenti, P.: A weather regime  
819 characterisation of winter biomass aerosol transport from southern Africa, *Atmos. Chem.*  
820 *Phys.*, 21, 16575–16591, <https://doi.org/10.5194/acp-21-16575-2021>, 2021.

821 Giorio, C., Doussin, J. F., D'Anna, B., Mas, S., Filippi, D., Denjean, C., Mallet, M. D.,  
822 Bourriane, T., Burnet, F., Cazaunau, M., Chikwililwa, C., Desboeufs, K., Feron, A., Michoud,  
823 V., Namwoonde, A., Andreae, M. O., Piketh, S. J. and Formenti, P.: Butene Emissions From  
824 Coastal Ecosystems May Contribute to New Particle Formation, *Geophys. Res. Lett.*, 49(10),  
825 [doi:10.1029/2022GL098770](https://doi.org/10.1029/2022GL098770), 2022.

826 Hamilton, D. S., Perron, M. M. G., Bond, T. C., Bowie, A. R., Buchholz, R. R., Guieu, C., Ito,  
827 A., Maenhaut, W., Myriokefalitakis, S., Olgun, N., Rathod, S. D., Schepanski, K., Tagliabue,  
828 A., Wagner, R., and Mahowald, N. M.: Earth, Wind, Fire, and Pollution: Aerosol Nutrient  
829 Sources and Impacts on Ocean Biogeochemistry, *Annual Review of Marine Science*, 14, 303–  
830 330, <https://doi.org/10.1146/annurev-marine-031921-013612>, 2022.

831 Heine, K. and Völkel, J., Clay Minerals in Namibia and their Significance for the Terrestrial and  
832 Marine Past Global Change Research, *African Study Monographs. Supplementary Issue.*, 40,  
833 31-50, publisher The Research Committee for African Area Studies, Kyoto University, 2010.

834 [Hossein, M., Rwiza, M. J., Nyanza, E. C., Bakari, R., Ripanda, A., Nkrumah, S., Selemani, J.](#)  
835 [R., and Machunda, R. L.: Fluoride contamination a silent global water crisis: A Case of Africa.](#)  
836 [Scientific African, 26, e02485, <https://doi.org/10.1016/j.sciaf.2024.e02485>, 2024.](#)

837 Inness, A., Ades, M., Agustí-Panareda, A., Barré, J., Benedictow, A., Blechschmidt, A.-M.,  
838 Dominguez, J. J., Engelen, R., Eskes, H., Flemming, J., Huijnen, V., Jones, L., Kipling, Z.,  
839 Massart, S., Parrington, M., Peuch, V.-H., Razinger, M., Remy, S., Schulz, M., and Suttie, M.:  
840 The CAMS reanalysis of atmospheric composition, *Atmos. Chem. Phys.*, 19, 3515–3556,  
841 <https://doi.org/10.5194/acp-19-3515-2019>, 2019.

842 Klopper, D., Formenti, P., Namwoonde, A., Cazaunau, M., Chevaillier, S., Feron, A., Gaimoz,  
843 C., Hease, P., Lahmidi, F., Mirande-Bret, C., Triquet, S., Zeng, Z. and Piketh, S. J.: Chemical  
844 composition and source apportionment of atmospheric aerosols on the Namibian coast,  
845 *Atmos. Chem. Phys.*, 20(24), 15811–15833, doi:10.5194/acp-20-15811-2020, 2020.

846 Křibek, B., Nyambe, I., Sracek, O., Mihaljevič, M., and Knésl, I.: Impact of Mining and Ore  
847 Processing on Soil, Drainage and Vegetation in the Zambian Copperbelt Mining Districts: A  
848 Review, *Minerals*, 13, 384, doi:10.3390/min13030384, 2023.

849 Jordi, A., Basterretxea, G., Tovar-Sánchez, A., Alastuey, A., and Querol, X.: Copper aerosols  
850 inhibit phytoplankton growth in the Mediterranean Sea, *Proc. Nat. Acad. Sci.*, 109, 21246-  
851 21249, doi:10.1073/pnas.1207567110, 2012.

852 Journet, E., K. Desboeufs, S. Caquineau, & J.L. Colin, Mineralogy as a critical factor of dust  
853 iron solubility, *Geophys. Res. Letters*, 35, doi:10.1029/2007GL031589, 2008.

854 Li, W., Xu, L., Liu, X., Zhang, J., Lin, Y., Yao, X., Gao, H., Zhang, D., Chen, J., Wang, W.,  
855 Harrison, R. M., Zhang, X., Shao, L., Fu, P., Nenes, A., and Shi, Z.: Air pollution – aerosol  
856 interactions produce more bioavailable iron for ocean ecosystems, *Sci. Adv.*, 3, e1601749,  
857 <https://doi.org/10.1126/sciadv.1601749>, 2017.

858 Liebenberg-Enslin, H., von Oertzen, D., and Mwananawa, N.: Dust and radon levels on the  
859 west coast of Namibia – What did we learn?, *Atmos. Poll. Res.*, 11, 2100-2109,  
860 <https://doi.org/10.1016/j.apr.2020.05.020>, 2020.

861 Lohmeier, S., B. G. Lottermoser, K. Strauß, T. Adolffs, S. Sindern, D. Gallhofer, Nearshore  
862 marine garnet and magnetite placers in the Erongo and S-Kunene regions, Namibia, *Journal*  
863 *of African Earth Sciences*, 180, 104221, <https://doi.org/10.1016/j.jafrearsci.2021.104221>,  
864 2021.

865 Mahowald, N.M., D. S. Hamilton, K., R. M. Mackey, J. K. Moore, A. R. Baker, R. A. Scanza,  
866 and Y. Zhang, Aerosol trace metal leaching and impacts on marine microorganisms, *Nat.*  
867 *Commun.*, 5, 9, 2614, 10.1038/s41467-018-04970-7, 2018.

868 Mänd, K., Kirsimäe, K., Lepland, A., Crosby, C., Bailey, J., Konhauser, K., Wirth, R., Schreiber,  
869 A., and Lumiste, K.: Authigenesis of biomorphic apatite particles from Benguela upwelling zone  
870 sediments off Namibia: The role of organic matter in sedimentary apatite nucleation and  
871 growth, *Geobiology*, 16, 10.1111/gbi.12309, 2018.

872 Martínez-Alonso, S., Veeffkind, J. P., Dix, B., Gaubert, B., Theys, N., Granier, C., et al., S-  
873 5P/TROPOMI-derived NO<sub>x</sub> emissions from copper/cobalt mining and other industrial activities  
874 in the Copperbelt (Democratic Republic of Congo and Zambia). *Geophys. Res. Lett.*, 50,  
875 e2023GL104109. <https://doi.org/10.1029/2023GL104109>, 2023.

876 Meter, S. L., P. Formenti, S. J. Piketh, H. J. Annegarn, and M. A. Kneen, PIXE investigation of  
877 aerosol composition in the Zambian Copperbelt, *Nucl. Inst. and Meth.*, B150, 433–438, 1999.

878 Micella, I., Kroeze, C., Bak, M. P., and Stokal, M.: Causes of coastal waters pollution with  
879 nutrients, chemicals and plastics worldwide, *Marine Pollution Bulletin*, 198, 115902,  
880 <https://doi.org/10.1016/j.marpolbul.2023.115902>, 2024.

881 Michalowicz, A., Moscovici, J., Muller-Bouvet, D., and Provost, K.: MAX: Multiplatform  
882 Applications for XAFS, *Journal of Physics Conference Series (Online)*, 190, 4,  
883 Doi:101088/1742-6596/190/1/012034, 2009.

884 Mileusnić, M., Mapani, B. S., Kamona, A. F., Ružičić, S., Mapaure, I., and Chimwamurombe,  
885 P. M.: Assessment of agricultural soil contamination by potentially toxic metals dispersed from  
886 improperly disposed tailings, Kombat mine, Namibia, *J. Geochemical Exploration*, 144, 409-  
887 420, <https://doi.org/10.1016/j.gexplo.2014.01.009>, 2014.

888 Mitra, A., and Rimstidt, J. D.: Solubility and dissolution rate of silica in acid fluoride solutions,  
889 *Geochimica et Cosmochimica Acta*, 73, 7045-7059, <https://doi.org/10.1016/j.gca.2009.08.027>,  
890 2009.

891 Mwaanga, P., Silondwa, M., Kasali, G., and Banda, P. M.: Preliminary review of mine air  
892 pollution in Zambia, *Heliyon*, 5, e02485, <https://doi.org/10.1016/j.heliyon.2019.e02485>, 2019.

893 Nekhoroshkov, P., Bezuidenhout, J., Zinicovscaia, I., Yushin, N., Vergel, K., and Frontasyeva,  
894 M.: Levels of Elements in Typical Mussels from the Southern Coast of Africa (Namibia, South  
895 Africa, Mozambique): Safety Aspect, *Water*, 13, 3238, 2021.

896 Nyanganyura, D., Maenhaut, W., Mathuthu, M., Makarau, A., and Meixner, F. X.: The chemical  
897 composition of tropospheric aerosols and their contributing sources to a continental  
898 background site in northern Zimbabwe from 1994 to 2000, *Atmos. Environ.*, 41, 2644-2659,  
899 <https://doi.org/10.1016/j.atmosenv.2006.11.015>, 2007.

900 Omoregie E., E. C. Vellemu, F. Nashima, B. Mudumbi Samona Brian, G. Liswaniso Gadaffi  
901 and K. Shimooshili, Assessment of copper levels along the Namibian marine coastline, *GSC*  
902 *Biological and Pharmaceutical Sciences*, 7, 48-55,  
903 <https://doi.org/10.30574/gscbps.2019.7.3.0101>, 2019.

904 Onjefu, S. A., Shaningwa, F., Lusilao, J., Abah, J., Hess, E., and Kwaambwa, H. M.:  
905 Assessment of heavy metals pollution in sediment at the Omaruru River basin in Erongo  
906 region, Namibia, *Environ. Poll. Bioavailability*, 32, 187-193, 10.1080/26395940.2020.1842251,  
907 2020.

908 Onipe, T., Edokpayi, J. N., and Odiyo, J. O.: A review on the potential sources and health  
909 implications of fluoride in groundwater of Sub-Saharan Africa, *Journal of Environmental*  
910 *Science and Health, Part A*, 55, 1078-1093, 10.1080/10934529.2020.1770516, 2020.

911 Paatero, P., Least squares formulation of robust non-negative factor analysis. *Chemometrics*  
912 *and Intelligent Laboratory Systems*, 37(1), 23–35. [https://doi.org/10.1016/S0169-](https://doi.org/10.1016/S0169-7439(96)00044-5)  
913 [7439\(96\)00044-5](https://doi.org/10.1016/S0169-7439(96)00044-5), 1997.

914 Paatero, P., and Tapper, U., Positive matrix factorization: A non-negative factor model with  
915 optimal utilization of error estimates of data values. *Environmetrics*, 5(2), 111–126.  
916 <https://doi.org/10.1002/env.3170050203>, 1994

917 Paris, R. and K. Desboeufs, Effect of atmospheric organic complexation on iron-bearing dust  
918 solubility, *Atmos. Chem. Phys.*, 13, 4895–4905, doi:10.5194/acp-13-4895-2013, 2013.

919 Rakovan J.F., J.M.Hughes, Strontium in the apatite structure: strontian fluorapatite and  
920 belovite-(ce), *The Canadian Mineralogist*, 38 (4), 839–845, doi: 10.2113/gscanmin.38.4.839,  
921 2000.

922 Rajot, J.-L., P. Formenti, S. Alfaro, K. Desboeufs, S. Chevaillier, B. Chatenet, A. Gaudichet, E.  
923 Journet, B. Marticorena, S. Triquet, A. Maman, N. Mouget, and A. Zakou, AMMA dust  
924 experiment: An overview of measurements performed during the dry season special  
925 observation period (SOP0) at the Banizoumbou (Niger) supersite, *J. Geophys. Res.*,  
926 doi:10.1029/2008JD009906, 2008.

927 Rathod, S. D., Hamilton, D. S., Mahowald, N. M., Klimont, Z., Corbett, J. J., and Bond, T. C.:  
928 A Mineralogy-Based Anthropogenic Combustion-Iron Emission Inventory, *J. Geophys. Res.*,  
929 125, e2019JD032114, <https://doi.org/10.1029/2019JD032114>, 2020.  
930

931 Simpson, W. R., S. S. Brown, A. Saiz-Lopez, J. A. Thornton, and R. von Glasow, Tropospheric  
932 Halogen Chemistry: Sources, Cycling, and Impacts, *Chem. Rev.*, 115, 4035-4062, DOI:  
933 10.1021/cr5006638, 2015.

934 Skamarock, W. C., Klemp, J. B., Dudhia, J., Gill, D. O., Barker, D., Duda, M. G., Powers, J. G.,  
935 A Description of the Advanced Research WRF Version 3 (No. NCAR/TN-475+STR). University  
936 Corporation for Atmospheric Research. doi:10.5065/D68S4MVH, 2008.

937 Sracek, O., Wanke, H., Ndakunda, N. N., Mihaljevič, M., and Buzek, F.: Geochemistry and  
938 fluoride levels of geothermal springs in Namibia, *Journal of Geochemical Exploration*, 148, 96-  
939 104, <https://doi.org/10.1016/j.gexplo.2014.08.012>, 2015.

940 Sracek, O.: Formation of secondary hematite and its role in attenuation of contaminants at  
941 mine tailings: review and comparison of sites in Zambia and Namibia, *Frontiers in*  
942 *Environmental Science*, 2, 10.3389/fenvs.2014.00064, 2015.

943 Strain, E.M.A., Lai R.W.S., White C.A., Piarulli S., Leung K.M.Y., Airolidi L., and O'Brien A.,  
944 Editorial: Marine Pollution - Emerging Issues and Challenges. *Front. Mar. Sci.* 9:918984. doi:  
945 10.3389/fmars.2022.918984, 2022.

946 Sylvanus, O., Kgabi, N., and Taole, S.: Heavy Metal Seasonal Distribution in Shore Sediment  
947 Samples along the Coastline of Erongo Region, Western Namibia, *European Journal of*  
948 *Scientific Research*, 139, 49-63, 2016.

949 Tao, Y., Ye G, Zhang H, Hu Y, Zuo Q, Wang X, Zhu S, Kang X, Zhang Y, Xiang X, et al. Effect  
950 of Fluoride Ions on the Surface Dissolution of Vanadium-Bearing Biotite. *Separations*. 9, 422,  
951 <https://doi.org/10.3390/separations9120422>, 2022.

952 Ueda, S., Iwamoto, Y., Taketani, F., Liu, M., and Matsui, H.: Morphological features and water  
953 solubility of iron in aged fine aerosol particles over the Indian Ocean, *Atmos. Chem. Phys.*, 23,  
954 10117–10135, <https://doi.org/10.5194/acp-23-10117-2023>, 2023.

955 Usher, C. R., Michel, A. E., and Grassian, V. H.: Reactions on Mineral Dust, *Chemical*  
956 *Reviews*, 103, 4883-4940, 10.1021/cr020657y, 2003.

957 Yang, T., Chen, Y., Zhou, S., and Li, H.: Impacts of Aerosol Copper on Marine Phytoplankton:  
958 A Review, *Atmos.*, 10, 414, <https://doi.org/10.3390/atmos10070414>, 2019.

959 White, K., Walden, J., and Gurney, S. D.: Spectral properties, iron oxide content and  
960 provenance of Namib dune sands, *Geomorphology*, 86, 219-229,  
961 <https://doi.org/10.1016/j.geomorph.2006.08.014>, 2007.